

Award Accounts

The Chemical Society of Japan Award for Creative Work for 2003

Function Cultivation of Transparent Oxides Utilizing Built-In Nanostructure

Hideo Hosono,*[1,2] Toshio Kamiya,[2] and Masahiro Hirano[1]

[1]ERATO-SORST, In Frontier Collaborative Research Center, Tokyo Institute of Technology, Mail Box S2-13, 4259 Nagatsuta, Midori-ku, Yokohama 226-8503

[2]Materials and Structures Laboratory, Tokyo Institute of Technology, 4259 Nagatsuta, Midori-ku, Yokohama 226-8503

Received May 11, 2005; E-mail: hosono@msl.titech.ac.jp

This review article describes recent progress in our research on cultivation of functionality in crystalline and amorphous transparent oxides utilizing nanostructures embedded in the material itself. It includes the background of our research and approach. Subjects included are material exploration and device application of transparent oxide semiconductors for transparent electronics, function emergence in nano-porous crystal $12CaO \cdot 7Al_2O_3$ utilizing active anion species stabilized by sub-nanometer-sized cages, and modified silica glass for vacuum/deep ultraviolet lasers. Our description of each subject include: background and approach, material design concept, fabrication or modification method, properties, and device fabrication. Emphasis is placed on the importance of a variety of built-in nanostructures in transparent oxides for novel function realization and the high potential of transparent oxides as ingredients for an ubiquitous element strategy of material research in this century.

1. General Introduction

1.1 Research Background. The Clarke number shows the order in natural abundance of elements in the earth crust. The top ten are listed as oxygen, silicon, aluminum, iron, calcium, sodium, potassium, magnesium, hydrogen, and titanium. This means that our territorial environment consists of oxides of these abundant metals and water. Human beings have created civilization utilizing these oxides to date, i.e., Al_2O_3, SiO_2, CaO, and MgO for Stone Age, and Fe for Iron Age; the present Information Age is supported by Si-semiconductors and SiO_2-glass fibers. There is no doubt that the coming age will be created through utilizing these abundant materials intelligently.

Oxide ceramics are probably among the oldest of man-made materials owing to the abundance and easy availability of the ingredients. Although most oxides are optically transparent, important for optical applications, it has been believed that active functions based on "excited electrons," such as in crystalline semiconductor materials, are not possible. For example, alumina and glasses, which are representative oxides, are optically transparent but electrically insulating.

However, during the past two decades techniques to purify oxides have drastically advanced. It is now possible to obtain highly pure materials, resulting from concentrated studies on fine ceramics in the 1980s. For instance, metal oxide chemicals containing sub-ppm impurities are now commercially available. Furthermore, the thin film deposition technique of oxides has advanced through intensive studies on high *T*c superconductors for electronic applications in the last decade. Taking advantage of this situation, the research group headed by Hiroshi Kawazoe and Hideo Hosono of Tokyo Tech.[1] has explored transparent conducting oxides (TCOs) while following a working hypothesis established based on a consideration of chemical bonding and point defects, resulting in the discovery of more than ten new TCOs.[2] The important among them are p-type TCO, $CuAlO_2$, reported in Nature (1997) and a series of amorphous TCOs in which the Fermi-level is controllable by intentional doping (1996).[3] The former is particularly important because most active functions in semiconductors originate from pn-junctions. The absence of practical application of transparent oxide semiconductors is due primarily to the lack of a p-type TCO. It is therefore now possible to examine the possibility of *invisible circuits*[4] based on transparent oxides (Fig. 1). As for optical materials, Hosono et al.[5] reported novel photosensitive or photorefractive glasses, SiO_2 glasses,[6] and CaF_2 crystal[7] for excimer laser applications. These materials were found through accumulated fundamental research on defects in glass and dielectric crystals. This study started from October 1, 1999, under such a situation.

1.2 Research Concept and Strategy. A research concept "Transparent Electro-Active Materials (TEAM)" was born in a dream: "We wish to convert alumina to a transparent semiconductor." TEAM includes wide bandgap materials based on abundant oxides having active electronic functionality. Transparent oxides are the most abundant and stable materials on earth, and are environmentally friendly. Although they have

Published on the web January 13, 2006; DOI 10.1246/bcsj.79.1

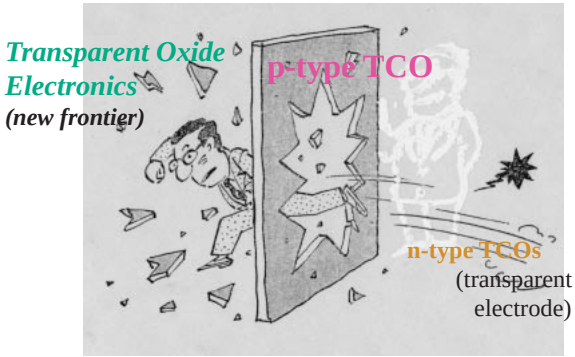

Fig. 1. Impact of discovery of p-type transparent conductive oxide.

been used as ingredients of traditional materials such as porcelain, cement, and glass, few active functions have been found in them. In fact, these materials are described as typical insulators in college textbooks. A widely accepted view "a transparent oxide cannot be a platform for electro-active materials" comes from phenomenological observation. One of the authors (HH) thinks it possible to realize a variety of active functionalities for transparent oxides by appropriate approaches based on an original view for these materials.

What is unique about transparent oxides? We think there are two characteristic features: One is that a wide variety of crystal structures and constituting elements are characteristic of oxides. No such a vast variety is seen in typical semiconductors or compound semiconductors. The crystal structure of the latter is limited to diamond-type. This striking difference arises from differences in chemical bonding nature between oxides and compound semiconductors, i.e., although ionic nature controlling a long range ordering is primary in oxides, covalent nature determining the local coordination structure contributes to the bonding significantly, depending on the type of metal cation. On the other hand, bonds in compound semiconductors are almost covalent and as a consequence local coordination configuration is tetrahedral.

Another factor is a variety of excited states. Although transparent oxides composed of abundant elements appear less interesting in the ground state, there are many interesting excited states. Representative examples are a self-trapped exciton which works as an energy localization center, leading to persistent defect formation, and a polaron composed of a charge carrier and its associated polarization and host lattice deformation field.[8] This feature provides valuable opportunities to modify transparent dielectric crystalline and amorphous oxides to gain novel functions and devices by electronic excitation.

In this study, we focused on transparent oxides with low-dimensional structures or composed of nano-porous structures from the first view point (Fig. 2). Interesting optical and electrical properties originating from these unique crystal structures are expected to emerge.

Our approach to novel function studies in transparent oxides by electronic excitation via interesting excited states was taken from the second view point. Femtosecond (fs) laser and F_2 excimer laser were chosen as tools for modification by electronic excitation. Extremely high energy density pulses are available from a table top fs-laser through a regenerative amplification.

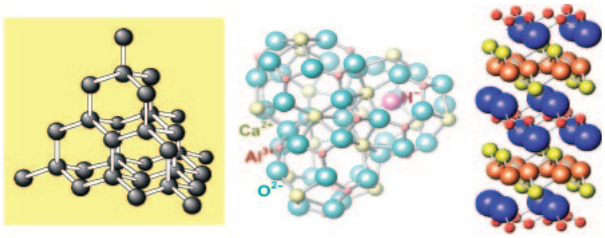

Fig. 2. Crystal Structure. (left) Diamond-type, (middle) nano-cage-type, and (right) layer-type.

So far, transparent dielectrics are unfavorable for laser machining because most photons pass through the sample. Fs laser pulse resolves this difficulty due to large nonlinear effects arising from extremely high peak power, it thus provides an opportunity to write 3-dimensional optical integrated circuits in transparent oxides. Vacuum ultraviolet laser pulse is a new radiation for transparent oxides. Little knowledge on the interaction of F_2-laser pulse (wavelength: 157 nm) with transparent oxides has accumulated to date notwithstanding the facts that applications to next-generation optical lithography in semiconductor chip manufacturing are emerging and potential applications to bio-related fields are being suggested. This area may be regarded as frontier of optical materials.

In summary, we choose transparent oxides with unique crystal structures and/or electronic structures and explore the novel active functions by utilizing state-of-the art facilities. The primary purpose is to explore intrinsic potential of transparent oxides as functional materials toward the cultivation of new materials frontier. Emphases are placed on establishment of new material view and new methodology, both of which may lead to effective and powerful tools for future study in this area.

The present study is composed of 3 major subjects; transparent oxide semiconductors, nano-porous crystalline oxides, and optical oxides for vacuum/deep ultraviolet lasers. The major achievements in each subject are described below.

2. Transparent Oxide Semiconductors

2.1 Background and Approach. It is believed that high optical transparency is in general incompatible with high electronic conduction, since optical transparency requires bandgaps larger than 3.3 eV while such a large gap makes carrier doping very difficult. In this sense, Transparent Conductive Oxides (TCOs) are unique materials. The first TCO developed was In_2O_3:Sn (ITO) in 1954, followed by findings of other TCOs; SnO_2 and ZnO. Now the TCOs are widely usedifor solar cells and flat-panel displays.

However, TCOs had been used only for passive applications such as window electrodes and transparent interconnections. It was because active devices such as pn junctions could not be fabricated due to absence of p-type TCO. The breakthrough was the finding of the first p-type TCO $CuAlO_2$ in 1997 by our group,[1] which triggered the development of a series of p-type TCOs and transparent pn-junction devices such as UV LEDs. These achievements changed our conception of TCOs to Transparent Oxide Semiconductors (TOSs), and therefore, we consider that TOSs have potential to develop new functional optoelectronic devices that the present Si-based semiconductor technology cannot.

In our study, we first discussed how to design new TOSs based on knowledge about electronic structures accumulated experimentally and theoretically. The validity of our material design concepts was demonstrated by developing new TOSs including p-type TOSs. These new TOSs led to transparent electronic devices such as UV LEDs and transparent TFTs.

We concentrated on development of new functions and realization of new devices utilizing natural nanostructures embedded in crystal structures of TOSs. Although we did not achieve satisfactory results yet, we have found unique optoelectronic properties associated with low-dimensional electronic structures in layered oxychalcogenides and have developed bright light-emitting devices using a nano-porous semiconductor C12A7:e^-.

2.2 Our Guiding Principle for Developing New TOSs. Conduction band minimum (CBM) of many metal oxides is made of spatially-spread isotropic metal s orbitals. Therefore, electrons in the metal oxides can have small effective masses, so high electronic conduction is possible if high-density electron doping is attained. This is the reason why several n-type TOSs have been found to date. In contrast, the valence band maximum (VBM) is made of oxygen 2p orbitals, which are rather localized and cause large hole effective masses. The dispersion of valence band tends to be small, so the VBM level is rather deep and hole doping is difficult; therefore, p-type TOS had not been found before 1997. We proposed an idea that the use of metal d orbitals with energy levels close to those of O 2p may form highly hybridized orbitals with O 2p. We expected that it might raise VBM and make hole doping easier. We noticed that the Cu^+ $3d^{10}$ configuration was a candidate because the Cu 3d energy levels are just above the O 2p levels and the closed shell configuration of Cu^+ allows large bandgaps and optical transparency. It actually led to the finding of $CuAlO_2$.[1] This was followed by the subsequent findings of new Cu^+-based p-type TOSs such as $CuGaO_2$ and $SrCu_2O_2$. In 2001, first bipolar TOS, $CuInO_2$,[42] was discovered.

However, high-concentration hole doping has not been achieved and the hole mobilities are not large enough in these Cu^+-based p-type TOSs. Therefore, the material design concept was extended to chalcogenides. What we intended was to increase the valence band dispersion by forming hybridized orbitals with chalcogen p orbitals that are more delocalized than O 2p. We preferred layered oxychalcogenides because they are optically transparent although simple chalcogenides are usually opaque.

Amorphous TOSs are another interest because, as noted above, electron-transport paths (i.e. CBMs) of TOSs are made of isotropic spread metal s orbitals. It results in unique carrier-transport properties in amorphous TOSs: i.e. large electron Hall mobilities (e.g. $>20\,cm^2\,V^{-1}\,s^{-1}$) comparable with those of corresponding crystalline materials may be attained, which is different from covalent amorphous semiconductors such as amorphous hydrogenated silicon (a-Si:H).

2.3 Research Topics. 2.3.1 Novel Functional TOSs: 2.3.1.1 p-Type TOSs: Cu^+-Bearing Oxides; In 1997, we reported $CuAlO_2$ thin films as a first p-type TOS along with a chemical design concept for exploring p-type TOSs.[1,2] After that, a series of p-type TOSs based on Cu^+-bearing oxides such as $CuGaO_2$[9] and $SrCu_2O_2$[10] have been found.

In order to clarify the origin of p-type conduction, the electronic structure of $SrCu_2O_2$ was examined by photoelectron spectroscopy and band structure calculations using LDA.[11] The electronic structure around the bandgap was found similar to that of Cu_2O, despite a large difference in the bandgap energies. That is, the admixed orbitals of 3d, 4s, and 4p of Cu^+ ion are hybridized with 2p orbital of ligand O^{2-} ions, which constitutes the VBM.

2.3.1.2 Alternative p-Type TOSs: $ZnRh_2O_4$; It is known that transition-metal ions with $4d^6$ configurations located in the octahedral crystal field have a low-spin configuration at the ground state, which may be regarded as "quasi-closed shell" configuration. Based on an idea that such ions are expected to behave similar to Cu^+ ions with the $3d^{10}$ closed shell configuration and to enhance the dispersion of valence band, we have found that normal spinel $ZnRh_2O_4$ is a p-type wide-gap semiconductor with a bandgap of $\sim$2.1 eV.[12] The electrical conductivity of the sputtered film was $0.7\,S\,cm^{-1}$ at 300 K without intentional doping. The magnetic susceptibility, photoelectron spectroscopy, and optical measurements revealed that the bandgap originated from the ligand-field split of Rh^{3+} d orbitals in octahedral symmetry, where the valence bands were made of fully occupied $t_{2g}{}^6$ and the conduction band of empty $e_g{}^0$.

2.3.1.3 Deep-UV (DUV) TOS: β-Ga_2O_3; Conventional TCOs such as ITO and ZnO are opaque for DUV light (<300 nm) due to a small bandgap ($\sim$3 eV), although the DUV region will be important for future biotechnologies such as DNA detection. DNA detection may be possible by electrical sensing or DUV optical absorption measurements. It is necessary to improve molecular selectivity to realize the DNA detection function. Our idea is to control the selectivity by applying voltages to the adsorption surface. Therefore, DUV-transparent TCOs are needed for these applications.

It is considered that β-Ga_2O_3 is a good candidate because this material has a large bandgap of 5 eV, good electronic conduction of bulk single-crystal β-Ga_2O_3 was reported.[13] We successfully fabricated conductive β-Ga_2O_3 thin films by high-temperature pulsed-laser deposition at 880 °C[14] and subsequently succeeded in fabricating the conductive films at 300 °C by fine tuning the deposition conditions.[15] The optical bandgap estimated from the $(\alpha h\nu)^2$-$h\nu$ plot was 4.9 eV.

2.3.1.4 Transparent Electrochromic Material: NbO_2F; We demonstrated[16] that oxyfluoride NbO_2F with a ReO_3-type structure was a promising electrochromic material with a large bandgap energy. Diffuse reflectance spectra revealed that the optical bandgap of NbO_2F (3.1 eV) was larger than that of a well-known electrochromic oxide WO_3 (2.6 eV). Electronic conduction is rendered by heating at 500 °C in H_2 atmosphere with Pt powders. The sintered sample was blue and its electrical conductivity was $6 \times 10^{-3}\,S\,cm^{-1}$ at room temperature. The electrical conductivity decreased with increasing the temperature, exhibiting semiconductor behavior. A reversible electrochromism between pale-blue and deep-blue was confirmed in H_2SO_4 and Na_2SO_4 aqueous solutions.

2.3.1.5 Amorphous TOSs; Amorphous transparent oxide semiconductors (a-TOSs) have potential as transparent electrodes for flat-panel displays such as plastic or film LCDs and OLEDs, provided that a reasonably low-electrical resistivity can be obtained. The vacant ns orbitals of metal ions with an

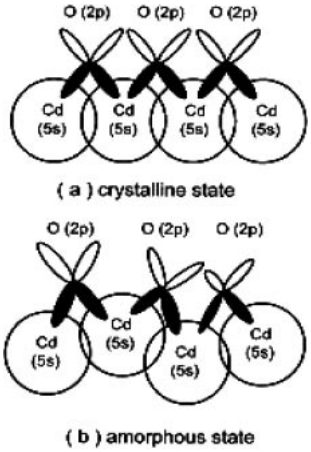

Fig. 3. Schematic illustration of electron-transport paths in (a) crystalline and (b) amorphous $2CdO \cdot GeO_2$.

electronic configuration of $(n-1)d^{10}ns^0$ ($n \geq 5$) are expected to form mobile carrier-transport paths even in amorphous structures. The recent discovery of new a-TOSs supports this expectation.[3] These a-TOSs are characterized by a high electron mobility ($\sim 10\,cm^2\,V^{-1}\,s^{-1}$), which is remarkably large compared to that of a-Si ($<1\,cm^2\,V^{-1}\,s^{-1}$).[17] The origin of the carrier-transport properties was theoretically clarified using the amorphous $2CdO–GeO_2$ system as an example.[18] The CBM is mainly composed of Cd 5s orbital, which is overlapped as illustrated in Fig. 3. Thus, high electron mobility originates from continuous electron conduction paths formed by direct overlapping of the Cd 5s orbitals.

However, amorphous TOSs containing Cd cannot be used for practical applications. We employed the $In_2O_3–Ga_2O_3–(ZnO)_m$ system instead of ZnO to clarify whether the 4s orbital has the ability to form a conduction path in an amorphous phase, since amorphous ZnO cannot be formed by a conventional film deposition process. In this system, In and/or Ga ions are expected to act as network formers. As a result, it was confirmed that the resultant films with $m = 1–4$ were amorphous and exhibited electrical conductivity of the order of $10^2\,S\,cm^{-1}$ and visible transparency.[19]

We found that amorphous films of Zn–Rh–O exhibit p-type conductivity. This is the first demonstration of p-type amorphous TOS. Amorphous oxide pn-junction diode with a good performance was also successfully fabricated using amorphous oxides of Zn–Rh–O and In–Ga–Zn–O.[20]

2.3.2 Growth Techniques for High-Quality Epitaxial Films: 2.3.2.1 Pulsed-Laser-Deposition: Super Flat ITO Epitaxial Films;[27] High-quality epitaxial films are necessary to study the intrinsic properties of electronic materials. We have developed several techniques for growing high-quality epitaxial films of TOSs using pulsed-laser deposition (PLD). For example, very low resistive ($7.8 \times 10^{-5}\,\Omega\,cm$, the world record) ITO epitaxial films were reproducibly grown on an atomically flattened (100)-YSZ single-crystal substrate at 600 °C (Fig. 4).[21] We also fabricated single-crystalline ITO films having an atomically flat surface ($R_{rms} \sim 0.2\,nm$ @ $1 \times 1\,cm^2$) on (111) surface of YSZ at 900 °C.[22] This atomically flat ITO worked as the base of successful fabrication of transparent pn-junctions,[23,24] near UV-emitting diode,[25] UV-detector,[26] and transparent organic TFT.[27,28]

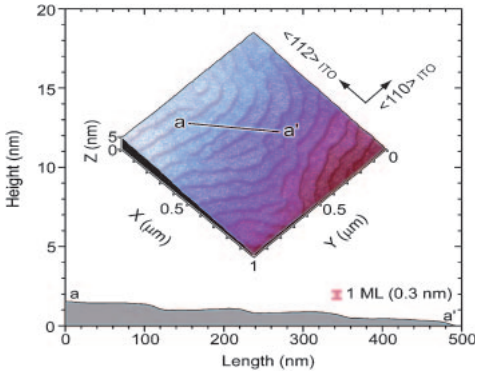

Fig. 4. AFM image of super-flat ITO thin films. A step corresponding to a monolayer of ITO is clearly seen.

2.3.2.2 Lateral Epitaxial Growth of Vanadyl-Phthalocyanine (VOPc) on Atomically Flattened ITO Film; We obtained a laterally grown VOPc layer on an epitaxial ITO film surface composed of atomically flat terraces and 0.29-nm-high steps using a molecular beam epitaxy (MBE) method.[27,28] The VOPc (phase II) layer was heteroepitaxially grown on the (111) ITO surface with a relationship of (010){21-2} VOPc ‖ (111){110} ITO. Crystallographic orientation of the film differs distinctly from those of the films grown on the other substrates such as alkali halides. AFM images revealed that six kinds of two-dimensional VOPc domains were heteroepitaxially grown laterally on the ITO surface and contacted with each other, forming domains and domain boundaries structures. These results demonstrate, by taking VOPc as an example, that the transparent conductive epitaxial ITO film with the atomically flat and stepped surface is effective to grow organic molecules laterally. The laterally-grown organic molecules on transparent conductive substrates are important for the emerging molecular electronics technology. Further, epitaxial layers of VOPc on ITO films would provide new information to clarify the mechanism of the improved hole injection in OLEDs.

2.3.2.3 Reactive Solid-Phase Epitaxy (R-SPE);[29] It is extremely hard to grow single-crystalline thin films of complex oxides, especially those having layered structures, by a conventional vapor-phase epitaxy. We developed a practical method to fabricate single-crystalline thin films of layered complex oxides, naming "Reactive Solid-Phase Epitaxy (R-SPE)."[29] First, the epitaxial template layer is grown on a substrate, followed by a deposition of a polycrystalline or amorphous film of complex oxides having a desired chemical composition. Single-crystalline films can be obtained if the bi-layer film is annealed in an appropriate atmosphere.

For example, $InMO_3(ZnO)_m$ (M = Al, In, and Ga; m = integer) has very unique layered structure, which is composed of alternate stacking of InO_2^- layers and $MO(ZnO)_m^+$ blocks. Single-crystalline films of $InGaO_3(ZnO)_m$ were grown by R-SPE as follows. A bi-layer film, which is composed of a 2-nm-thick ZnO epitaxial layer and amorphous $InGaO_3(ZnO)_5$, were annealed at 1400 °C in a furnace. A high-resolution transmission electron microscopic (HRTEM) image indicated that the film was single-crystalline $InGaO_3(ZnO)_5$ (Fig. 5). The epitaxial ZnO thin layer plays an essential role in controlling the crystallographic orientation, while the thickness ratio between

the two layers controls the film composition.

2.3.3 Novel Transparent p-Type Semiconductors: Layered Oxychalcogenides LnCuOCh (Ln = lanthanide, Ch = chalcogen): As already noted, we first reported a transparent p-type oxide semiconductor, $CuAlO_2$ in 1997 along with a material design concept[1,2] that selection of an appropriate cation that forms strong hybridization with O 2p will lead to good p-type conduction in TOSs. To meet optical transparency, Cu^+ ions were chosen to form the Cu^+-based p-type TOSs. Furthermore, as S 3p and Se 4p are more extended than O 2p, improved hole mobility was expected for oxychalcogenides. Considering these material design concepts, we found novel transparent p-type semiconductors, layered oxychalcogenides LnCuOCh (Ln = lanthanide, Ch = chalcogen).[30–32]

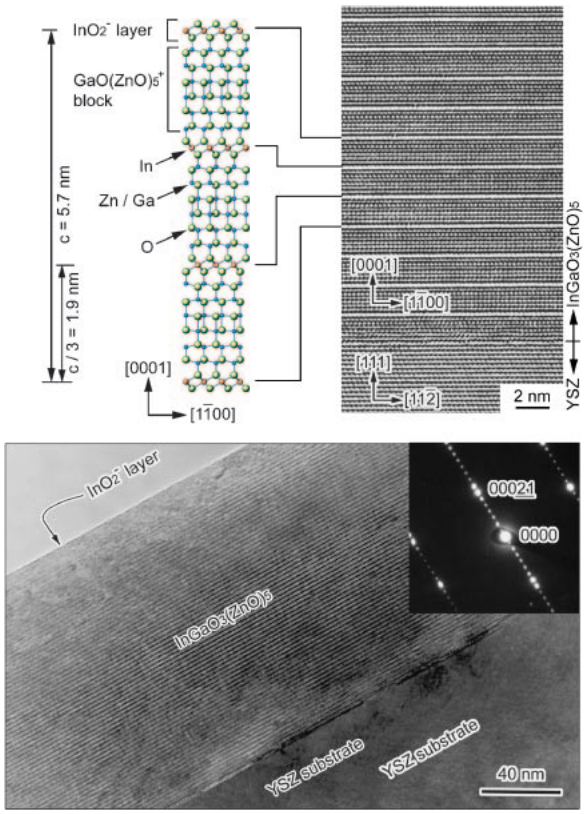

Fig. 5. Cross-sectional HRTEM image of $InGaO_3(ZnO)_5$ single-crystalline film fabricated by R-SPE method.

The crystal structure of LnCuOCh consists of mono-molecular oxide $(Ln_2O_2)^{2+}$ and chalcogenide $(Cu_2Ch_2)^{2-}$ layers alternately stacked along the *c*-axis (Fig. 6a).[33] Unique electrical and optical properties are expected for these layered oxychalcogenides due to the two-dimensional structure.

2.3.3.1 Heteroepitaxial Growth of LnCuOCh by R-SPE;[34,35] Like $InGaO_3(ZnO)_m$, the chemical composition of LnCuOCh is relatively complex, and the chalcogenide component, Cu_2Ch, evaporates easily from the film at high temperatures in vacuum. The evaporation of Cu_2Ch results in the deviation of chemical composition from stoichiometry, resulting in decomposition into Ln_2O_3, Ln_2O_2Ch, and Cu_2Ch. Although much effort has been spent to grow epitaxial LnCuOCh films at high temperatures by a PLD technique, heteroepitaxial films have not been obtained. Therefore, we employed the R-SPE technique to epitaxial growth of LnCuOCh. In this case, heteroepitaxial films of LnCuOCh were obtained when a thin Cu layer was used as a sacrificial layer.

First, thin sacrificial Cu (thickness ~5 nm) layers were deposited on (001)-oriented MgO substrates by the PLD technique. Then, amorphous LnCuOCh films were sequentially deposited on the Cu layers. Finally, the a-LnCuOCh/Cu bi-layer films were thermally annealed at 1000 °C in evacuated SiO_2 glass ampoules. After the thermal annealing, we obtained heteroepitaxially grown LnCuOCh (Ln = La, Ce, Pr, Nd; Ch = $S_{1-x}Se_x$, $Se_{1-y}Te_y$) films. A cross-sectional high-resolution transmission electron microscopic (Fig. 6b) image of the epitaxial LaCuOS film shows that layered patterns associated with the (00*l*) planes of LaCuOS are stacked parallel to the substrate surface over the whole area of the film. The sacrificial thin Cu layer deposited before the thermal annealing is needed to form seed grains for the epitaxial growth at triple junctions among the Cu, a-LaCuOS layer, and the substrate.[36]

2.3.3.2 Electrical Properties: "Natural" Modulation Doping and Transparent Degenerate Conductivity;[37] All the epitaxial LnCuOCh films exhibited p-type electrical conduction. Hall mobility becomes larger with an increase in the Se content, reaching 8.0 $cm^2 V^{-1} s^{-1}$ in LaCuOSe, which is a value comparable to that of p-type GaN:Mg. Mg doping increased the hole concentration up to 2×10^{20} cm^{-3}. The Hall mobility of the Mg-doped films is increased from 0.2 to 4.0 $cm^2 V^{-1} s^{-1}$ by anion substitution from S to Se, which increased the electrical conductivity from 5.9 to 140 S cm^{-1} (Fig. 7).

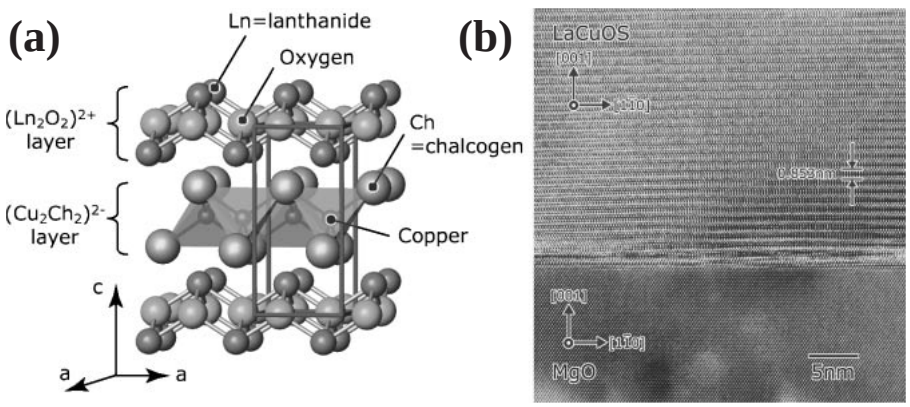

Fig. 6. Crystal structure (a) and HRTEM image (b) of LnCuOCh epitaxial thin film fabricated by R-SPE method.

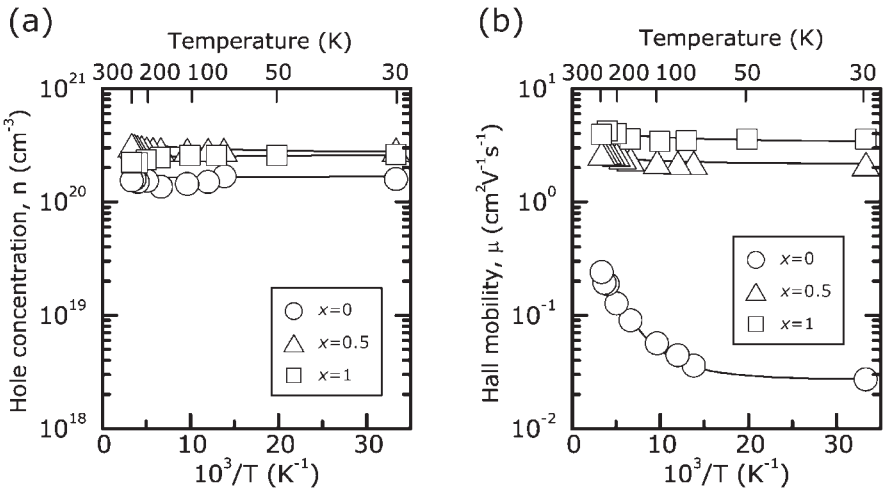

Fig. 7. Carrier-transport properties of Mg-doped $LaCuOS_{1-x}Se_x$ thin films. (a) Hole concentration and (b) Hall mobility.

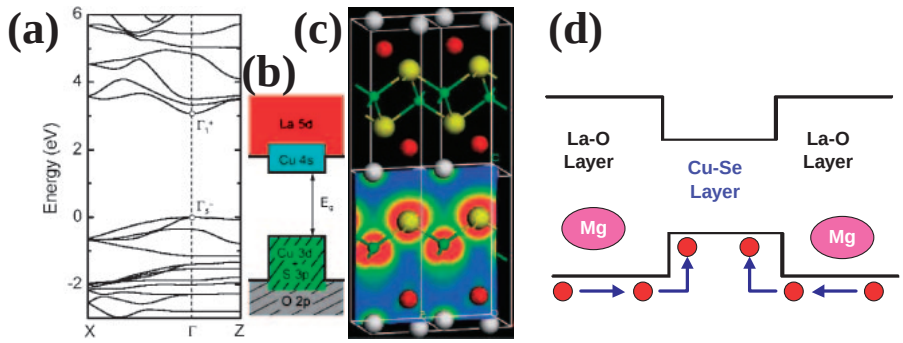

Fig. 8. Two-dimensional electronic structure in LaCuOCh. (a) Band structure, (b) schematic illustration of the electronic structure around the bandgap, (c) density contour map of electrons at the VBM, and (d) schematic illustration describing natural modulation doping.

It is noteworthy that the mobility of the Mg-doped films is reduced only to half of the undoped films despite the heavy Mg ion doping. The coexistence of the high hole concentrations $> 10^{20}\,cm^{-3}$ and the moderately large mobilities is unusual in conventional semiconductors. It may be attributed to the natural modulation doping, which corresponds to the layered crystal structure, i.e., Mg^{2+} ion doping generates hole carriers in the $(La_2O_2)^{2+}$ layer (carrier doping layer) and then the hole carriers generated are transferred to the $(Cu_2Ch_2)^{2-}$ layer (hole conduction layer) due to a large band offset at the VBM (Fig. 8d). Charged impurities do not scatter mobile hole carriers since the hole conduction layer is spatially separated from the doping layer, which naturally forms a modulation doping structure such as that formed artificially in a High Electron Mobility Transistor.

2.3.3.3 Optical Properties: Room Temperature Exciton and Two-Dimensional Electronic Structure;[38,39] The optical spectroscopic properties of LnCuOCh (Ln = La, Pr, and Nd; Ch = S or Se) on epitaxial films were examined and some unique optical properties were clarified. Free exciton emissions were observed from all the films between 300 K to ~30 K (Fig. 9). In addition, a sharp emission line, which was attributed to bound excitons, appeared below ~80 K. The exciton binding energies were evaluated to be ~50 meV for all LaCuOCh. It was confirmed that anionic and cationic substitutions tuned the emission energy from 3.21 to 2.89 eV (λ = 386–429 nm) at

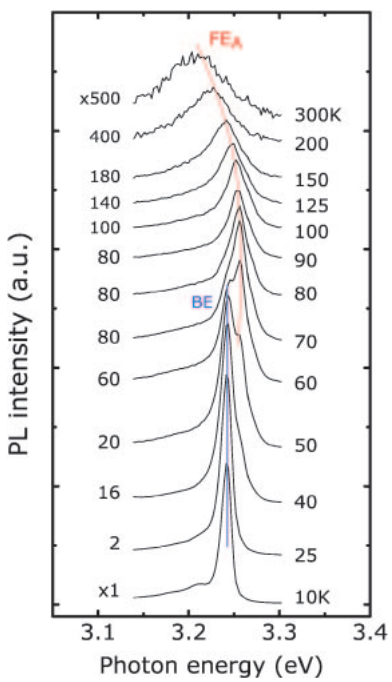

Fig. 9. Temperature dependence of excitonic photoluminescence from LaCuOS. EF_A and BE denote emission from free and bound excitons, respectively.

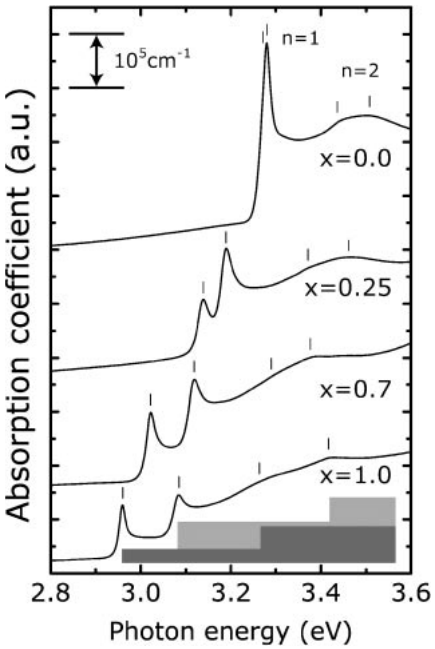

Fig. 10. Two-dimensional optical absorption spectra observed in $LaCuOS_{1-x}Se_x$. Step-like density of states arising from 2D-electronic nature is seen.

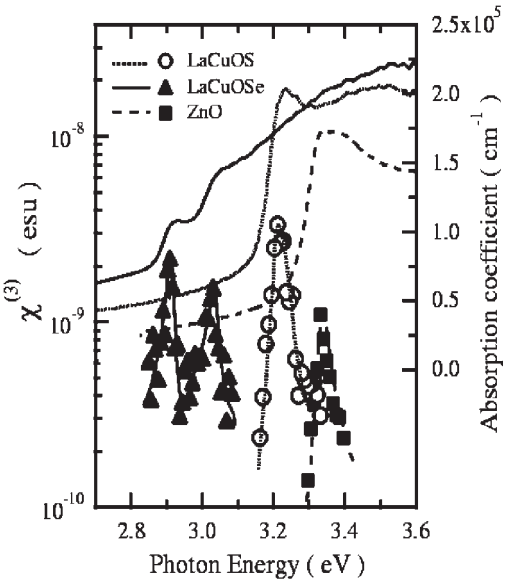

Fig. 11. The $\chi^{(3)}$ and absorption spectra of LaCuOS (dotted curve), LaCuOSe (solid curve), and ZnO (dashed curve) epitaxial thin films as a function of the excitation energy at room temperature.

300 K, which provides a way to engineer the electronic structure in light-emitting devices.

Step-wise absorption spectra with excitonic peak splitting due to the spin–orbit interaction of Ch ions experimentally verified that an exciton in the $(Cu_2Ch_2)^{2-}$ layers shows two-dimensional behavior (Fig. 10). Energy band calculations revealed that Cu–Ch hybridized bands only spread in the $(Cu_2Ch_2)^{2-}$ layers, which suggests that hole carriers in these bands are confined in the $(Cu_2Ch_2)^{2-}$ layers (Figs. 8a–c). The theoretical and experimental results indicate that LnCuOCh has "natural multiple quantum wells" built in the layered structure. The observed two-dimensional features of the step-wise shape with multi-level excitons in the optical absorption are unique to LnCuOCh. The step-wise exciton absorption has not been observed in other natural layered crystals that we have surveyed.

2.3.3.4 Optical Nonlinearity and Exciton–Exciton Interaction;[40,41] The confined excitons in nano-particle or nano-layered structures are expected to be stable and to cause a large optical nonlinearity around the resonant energies. Accordingly, we considered that LaCuOCh possess potentially large optical nonlinearity; such third-order optical susceptibility $\chi^{(3)}$ values were measured. Therefore, the spectral intensity and time response of $\chi^{(3)}$ on the epitaxial thin films of LnCuOCh were measured using a femtosecond time-resolved degenerative four-wave mixing (DFWM) technique around the bandgap energy. This method can also detect a small energy split as quantum beating appeared due to quantum interference between neighboring electronic levels.

The $\chi^{(3)}$ value for LaCuOS depends strongly on excitation energies and is resonantly enhanced to 4×10^{-9} esu at the absorption band peak (3.2 eV) (Fig. 11).

On the other hand, LaCuOSe has two absorption peaks (2.9 and 3.1 eV) corresponding to the valence band levels split by spin–orbit interaction. The $\chi^{(3)}$ values for LaCuOSe are enhanced at the peak energies up to $\sim 2 \times 10^{-9}$ esu, which are comparable to that for LaCuOS and larger than that for the ZnO film (1×10^{-9} esu) having larger exciton binding energy (60 meV). The $\chi^{(3)}$ values approach those for semiconductor CdS/Se nano-particles dispersed in a glass matrix. These large $\chi^{(3)}$ values in LaCuOCh are presumably attributable to increases in the density of exciton states caused by exciton confinement in the $(Cu_2Ch_2)^{2-}$ layer. The response time of the DFWM signals for LaCuOCh are 250–300 fs, corresponding to the phase decay time of 1–1.2 ps for excited excitons.

The DFWM signals for LaCuOS are also measured at 4 K with the excitation energies swept from 3.253 to 3.287 eV (Fig. 12b). The signals clearly exhibit beat structures for the laser energy of 3.266 eV (Fig. 12a), which is consistent with the peak energy of the exciton absorption band. The beat structures are attributed to the interference between the phases of polarized excitons separated by a small energy gap. The experimental data provide a beat period of 480 fs, which corresponds to the energy separation of 9 meV. These results clearly demonstrate that the absorption band for the exciton in LaCuOS consists of two separate excitonic states. The energy coincides well with the splitting energy obtained from ab-initio band calculations incorporating spin–orbit interaction. We could, therefore, verify that the valence band maximum state of LaCuOCh is composed of a pair of states split by spin–orbit interaction in Ch ions, and that the excitons in these states can interact with each other when they come across.

2.3.4 Device Applications: 2.3.4.1 Near UV-LED;[25] We realized that the near UV-emitting diode composed of pn-hetero-junction of TOSs, p-type $SrCu_2O_2$, and n-type ZnO. ZnO is an n-type TOS ($E_g = 3.38$ eV) which can emit UV ($\lambda = 380$ nm) due to room temperature exciton ($E_x = 59$ meV). Efficient electroluminescence centered at 382 nm was observed when a forward current was injected into the pn-hetero-junction diode

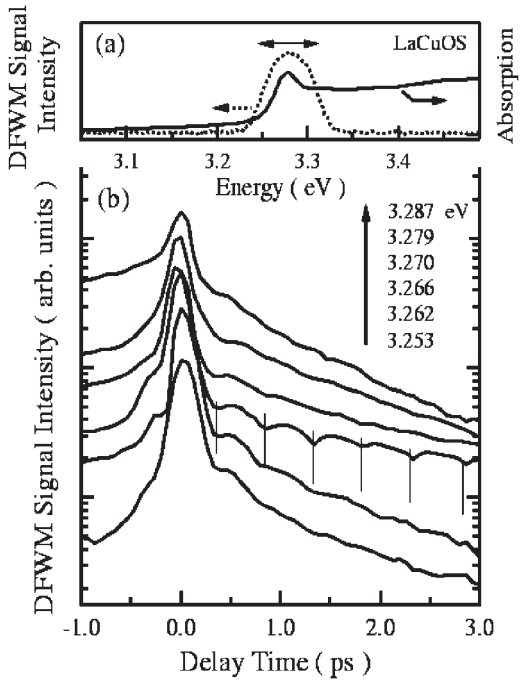

Fig. 12. (a) DFWM signal intensity (dotted curve) and absorption (solid curve) spectra of LaCuOS around the band-edge exciton. (b) DFWM traces for LaCuOS as a function of delay time for several excitation energies.

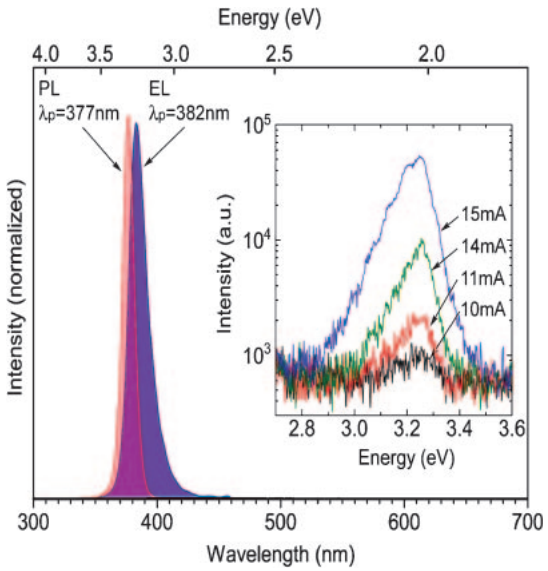

Fig. 13. Photoluminescence and current-injected luminescence spectra of p-$SrCu_2O_2$/n-ZnO hetero-junction LED. Inset shows EL spectra as a function of forward current injected to the junction.

(Fig. 13). The threshold voltage for electroluminescence was ~3 V, which evidenced that the origin of the electroluminescence was electron–hole recombination in the ZnO layer.

2.3.4.2 Transparent pn-Hetero-Junction Diode Fabricated by R-SPE;[26] pn-Hetero-junction diodes composed of wide-gap oxide semiconductors of p-$ZnRh_2O_4$ and n-ZnO were successfully fabricated by R-SPE. The pn-hetero-junction diodes

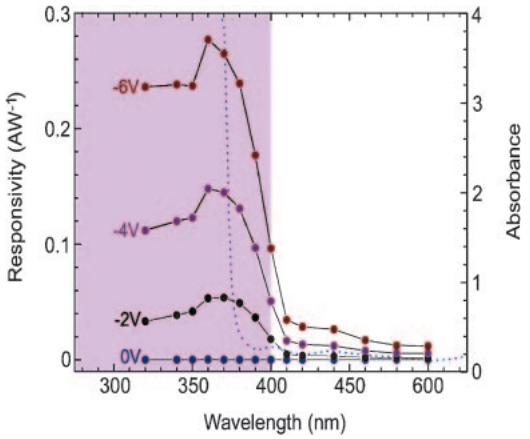

Fig. 14. Optical response of p-NiO/n-ZnO hetero-junction UV detector.

obtained have an abrupt interface and exhibit rectifying *I–V* characteristics with a threshold voltage of ~2 V, which is in good agreement with the bandgap energy of $ZnRh_2O_4$. It verifies that the hetero-junction formed by the narrow bandgap $ZnRh_2O_4$ and the wide bandgap ZnO works as a good carrier blocking contact. This behavior is similar to those of conventional pn-junctions, not specific to the d-electron system. On the other hand, with the irradiation of UV-light, the fundamental absorption edge of ZnO produces photovoltage more effectively than that of ~2 eV light, which may result from the intrinsic nature of the d-electron bands such as small absorption coefficient and less mobile carriers. We have demonstrated herein that the R-SPE is suitable for fabricating oxide hetero-junctions. This is an advantage point for fabricating optoelectronic devices using TOSs.

2.3.4.3 Transparent UV-Detector;[26] The ultraviolet (UV) radiation that reaches the Earth's surface is 280–400 nm in wavelengths (UV-A and UV-B); it plays a harmful role which may cause the skin cancer. A transparent UV-detector was fabricated by using a high-quality pn-hetero-junction diode composed of transparent oxide semiconductors, p-type NiO and n-type ZnO, and its UV-response was measured at room temperature. The diode exhibited clear rectifying *I–V* characteristic with the forward threshold voltage of ~1 V. Efficient UV-response was observed up to ~0.3 AW^{-1} at 360 nm (−6 V biased) (Fig. 14), which is comparable to that of commercial GaN detector.

2.3.4.4 Organic TFTs;[27,28] Transparent organic thin film transistors (OTFTs) were fabricated using the vanadyl-phthalocyanine (VOPc) film as an active p-channel, the lattice matched $(Sc_{0.7}Y_{0.3})_2O_3$ film as a high-*k* gate dielectric, and the atomically flat ITO film as a bottom contact. Lateral growth of the VOPc epitaxial channel layer on the epitaxial $(Sc_{0.7}Y_{0.3})_2O_3$ gate dielectric with root-mean-square (R_{rms}) roughness of ~1 nm was achieved by a molecular beam epitaxy (MBE) method. Laterally grown VOPc thin film contributes dominantly to obtaining a reasonably large field-effect mobility μ_{eff} of $\sim 5 \times 10^{-3}$ $cm^2\,V^{-1}\,s^{-1}$, which provides significant improvement compared with reported values of OTFT based on non-planar phthalocyanine. The present results also suggest that the bi-layered film composed of the lattice matched high-*k* gate

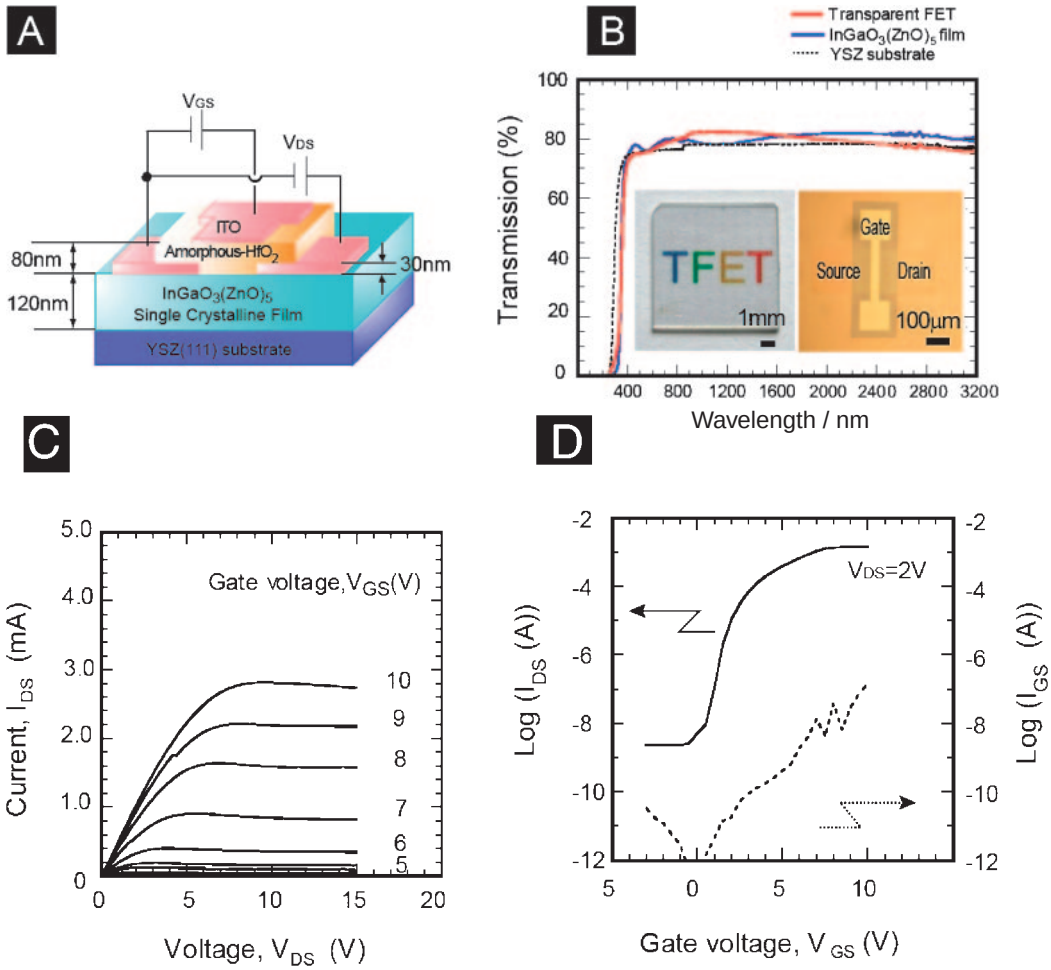

Fig. 15. Transparent TFT. (a) Device structure, (b) photo of a device chip, (c) output characteristics, and (d) transfer characteristic.

dielectric of Y–Sc–O system and the atomically flat ITO transparent electrode is applicable to other organic materials with larger mobility, leading to further improvement of transparent OTFTs.

2.3.4.5 High Performance Transparent TFTs;[43] Transparent thin film transistors (TTFTs), using TOSs as a channel layer have merits compared to conventional TETs when applied to flat-panel displays. The merits include an efficient use of back light in LCD and emitted light in OLED, and insensitiveness of device performance to visible light irradiation. In addition, TFTs based on oxides have potential advantages over conventional FETs in high voltage and high temperature tolerances. Although there have been several reports on the fabrication of TTFTs using conventional TOSs such as SnO_2 and ZnO,[44] their performances were not satisfactory for practical applications. The large off-current and the unintentional normally-on characteristics originate from the fact that these conventional TOSs contain many carriers in the as-prepared state due to a somewhat large nonstoichiometry in the chemical composition, i.e. oxygen vacancy, and it is hard to control the carrier density down to less than $10^{17}\,cm^{-1}$ without impurity counter doping. Their on/off current ratio and field-effect mobility (μ_{eff}) are as large as $\sim 5\,cm^2\,V^{-1}\,s^{-1}$, and the TFT characteristics exhibit "normally-on" characteristics unintentionally. In addition, as these TTFTs were fabricated in polycrystalline thin films, defects and grain boundaries in the active channel deteriorate the device performance.

The TOS-TTFT fabricated using a single-crystalline $InGaO_3(ZnO)_5$ film[29,45] displayed reasonable normally-off characteristics with good performance such as the large $\mu_{eff} \sim 80\,cm^2\,V^{-1}\,s^{-1}$, the low off current $\sim 10^{-9}$ A and the on/off current ratios larger than 10^5, distinguishing these materials from conventional TOS-TFETs reported to date. Figure 15a shows the device structure of the TTFT. An 80-nm-thick amorphous HfO_x layer was used for the gate insulator and transparent electrode of ITO was used for source, drain, and gate electrodes. The optical transmittance is almost 100% in the visible region (b). The output characteristics (c) shows source-to-drain current (I_{ds}) increases markedly as source-to-drain voltage (V_{ds}) increases at a positive gate bias V_{gs}, indicating that the channel is n-type and electron carriers are generated by positive V_{gs}. A large $\mu_{eff} \sim 80\,cm^2\,V^{-1}\,s^{-1}$ is obtained, estimated both from the transconductance value and from the saturation current. Off-current is very low, the order of 10^{-9} A and the on/off current ratios larger than 10^5 are obtained (d). These characteristics are greatly improved over those reported for TTFTs fabricated using conventional TOSs. The present achievement provides a practical method to fabricate TTFTs with reasonable performance, paving a way for realizing invisible circuits.

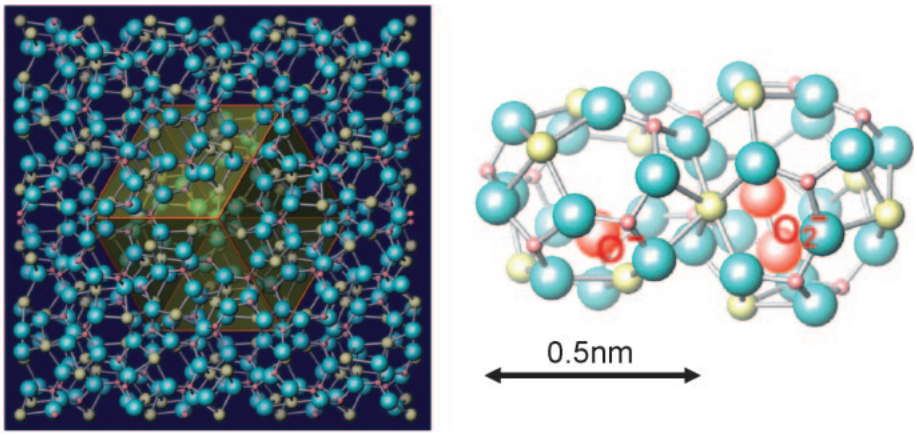

Fig. 16. Crystal structure of C12A7 (cubic lattice, viewed from ⟨111⟩ direction) and incorporation of anions (O^- and O_2^-) into cages. Since the lattice framework is positively charged (+1/3 per cage), the electroneutrality is preserved by the incorporation of the anions into the cages.

2.3.4.6 Field-Emission from C12A7:e^- and Application to FED;[46] $12CaO \cdot 7Al_2O_3$ (C12A7) is a unique material with the crystal structure composed of twelve positively-charged cages with ~0.4 nm in diameter. We found that new functions were added to C12A7 by replacing the clathrated free oxygen ions with other active anions. An electron may be regarded as an ultimate anion, and actually ~100% of the free oxygen ions may be replaced with the electron anions, forming a new inorganic electride C12A7:e^-. It exhibits large electronic conductivity up to 100 S cm^{-1}.

We examined the electron field emission from C12A7:e^-. It was observed that electron emission is controlled by thermionic emission at low extraction voltages, while Fowler–Nordheim (FN) field-emission dominates at voltages higher than 1500 V. The work function was estimated from the thermionic and FN emission models, both of which provide a value of ~0.6 eV. The electronic structure was also investigated by UPS, which gives a larger work function value of ~3.7 eV. We tentatively consider that the discrepancy in the work function arises from band bending due to partial oxidation near the surface.

The operation of field-emission display (FED) devices was also demonstrated. We fabricated FED devices using sodium salicylate or ZnO:Zn for phosphor, which exhibited bright light emission clearly visible in typical ambient light.

3. Transparent Nano-Porous Crystal $12CaO \cdot 7Al_2O_3$

3.1 Background and Approach. The guiding principles for designing functional metal-oxides such as semiconductors, magnetic materials, ionic conductors, high-temperature superconductors, and strong electron correlation compounds depend mostly on the selection of transition-metal or rare-earth ions. In contrast, main-group metal oxides, which are a major portion of traditional ceramics that are important for structural use, have not been expected to exhibit such functionalities except for good transparency and electrical insulation. However, since these oxides are abundant in nature and are environmentally benign, it is desirable that the functional materials containing rare or harmful metal elements are substituted with the main group metal oxides in order to guarantee the sustainable growth of our civilization. An ultimate goal of our study is, therefore, to revive the main-group metal oxides as functional materials. For this purpose, new strategies will be needed: Our strategies are an active use of the intrinsic nanostructure already inside these materials and the manipulation of the anions involved in them. These new strategies may provide novel functions to the environmental friendly oxides, which have not yet been realized by only utilizing heavy metal ions.

What we have focused on is a mixed main-group metal oxide, $12CaO \cdot 7Al_2O_3$ (C12A7), which is composed of only main-group elements with higher ranks in Clarke's abundance list (Ca: 5th, Al: 3rd, and O: 1st). C12A7 has been known as a constituent of alumina cements, and is typically a transparent (or white powder) and electrically insulating. Despite the apparent commonplaceness of C12A7, it has a distinct feature in its crystal structure. The unit cell under stoichiometric composition, $2[Ca_{12}Al_{14}O_{33}]$, may be represented as $[Ca_{24}Al_{28}O_{64}]^{4+} + 2O^{2-}$.[47] The former part, $[Ca_{24}Al_{28}O_{64}]^{4+}$, denotes a three-dimensional lattice framework which is illustrated in Fig. 16. The unit cell is composed of 12 cages with an inner free space of ~0.4 nm in diameter. Thus, the cage has a mean effective charge of +1/3 (=+4 charges/12 cages). The latter part, $2O^{2-}$, is referred to as "free oxygen" or "extra-framework oxide ion," and occupies 1/6 of the cage sites. The oxide ions can be partially or completely replaced by various monovalent anions such as OH^-, F^-, and Cl^-.[48] Such an anion-exchange property is complementary to conventional natural nanoporous crystals such as zeolites, whose lattice frameworks are principally formed with encaging cations.

Incorporation of unusual anions in the cages was first reported by Hosono and Abe,[49] who found the occurrence of superoxide ion (O_2^-) with a concentration of $\sim 1 \times 10^{19}$ cm^{-3} in C12A7 polycrystalline samples fabricated in air. This finding stimulated an examination of the ionic conduction properties of oxygen-related anions in C12A7, leading to a finding of fast O^{2-} ion conduction by Prof. West's group.[50] The free oxygen is believed to be responsible for the fast ionic conduction. It is also noteworthy that the composition of C12A7 easily forms a glass, which exhibits ultraviolet light-induced colorations due to the formation of point defects: Ozonide (O_3^-) and alumi-

num-oxygen hole center (Al-OHC) in the glass fabricated in an oxidizing atmosphere.[51] On the other hand, F^+-like centers are produced in the glass prepared in a reducing atmosphere, exhibiting phototropy.[52] Hence, an approach based on defects physics, anion chemistry, and thermodynamic analysis is effective in this material. Generally, our approach to render the C12A7 electro-active functions is based on the incorporation of chemically unstable, in other words, "active," negative species into the positively charged cage-structure inherent to this material by suitable thermal treatments or hot ion implantations. We employ a combination of conventional and state-of-the art characterization techniques including optical absorption, transient photoluminescence, Raman, continuous and pulsed wave EPR, NMR, TG mass spectroscopy, and muon spectroscopy. Such comprehensive characterization allows for better understanding of various novel phenomena discovered in C12A7.

To proceed materials research effectively, one needs samples of variable shapes. In particular, the single crystals were indispensable for studies of C12A7 such as ultraviolet light-induced electrical conductivity, the synthesis of an electride and clarification of the oxygen radical configuration in the cage. Theoretical calculation provides a solid basis to understand novel phenomena in C12A7, giving clear physical or chemical images to them. The adopted calculation technique, incorporation of quantum mechanical and fully relaxed embedded cluster, has an advantage that it treats such a crystal as having a "soft" framework structure that is deformed considerably when a specific ion species or an electron is encaged in the cage. Especially, the good theoretical analysis is needed to appropriately understand electronic and optical properties when doped with electrons into such a complicated crystal structure.[53]

3.2 Research Topics. 3.2.1 Fabrication of Translucent Ceramics, Single Crystals, and Thin Films: Fully densified translucent C12A7 ceramics were obtained by sintering hydrated C12A7 powders in a dry oxygen atmosphere at 1300 °C. The average transmittance between 400–800 nm for 1-mm-thick samples was improved up to ~70% by sintering for 48 h. Elimination processes of water molecules existing in pores was considered to play a crucial role in improving the transparency.[54]

We fabricated C12A7 single crystals by the floating zone method.[55] A conventional growth process resulted in the formation of a concave solid–liquid interface, leading to the formation of many bubbles and cracks in grown crystals. We have found that lowering the growth rate down to 1 mm/h significantly reduced the bubble generation. The suppression of the bubbles is very important, because their formation frequently disturbed the stability of the molten zone. Further, by introducing an alumina tube as a heat reservoir at the heating zone, the shape of the solid–liquid interface could be controlled to a convex shape, allowing for the growth of high quality crystals with higher growth rates.

Polycrystalline C12A7 thin films were prepared by the pulsed laser deposition of amorphous films on MgO substrates and subsequent annealing in oxygen atmosphere at temperatures above 800 °C.[56] The optical bandgap of C12A7 was evaluated to be 5.9 eV. Hydride ions were incorporated into the film by a thermal treatment in a hydrogen atmosphere at 1200 °C. The resulting transparent thin films were converted into transparent persistent electronic conductors exhibiting an electrical conductivity of $6.2 \times 10\,S\,cm^{-1}$ at 300 K by ultraviolet light illumination (Fig. 17).

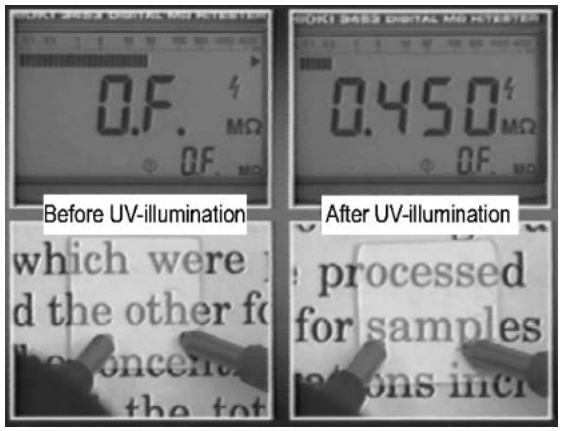

Fig. 17. Conversion from insulating to conductive states in an H^--incorporated C12A7 thin film (thickness: 200 nm) by ultraviolet light illumination. The color and the transparency of the film remains unchanged after by the conversion.

3.2.2 Formation of Abundant O^- and O_2^- Radicals:[57–61] It was found that extraordinarily high concentrations (the order of $10^{20}\,cm^{-3}$) of oxygen radicals, O^- and O_2^-, in C12A7 are formed in the cages by simply heating C12A7 ceramics in a dry oxygen atmosphere. The resultant C12A7 had outstanding oxidation reactivity such that even Pt metal can be oxidized into +4 charge state when the metal is put on the material at high temperatures. The formation of the oxygen radicals was decreased with decreasing oxygen partial pressure and increasing water vapor pressure during the heating.

The effect of oxygen partial pressure up to 400 atoms on the generation of active oxygen radicals in C12A7 was examined using a hot isostatic pressing furnace. Concentrations of O_2^- and O^-, which were analyzed from a combination of electron paramagnetic spin resonance (EPR) and Raman spectroscopy, increased with the oxygen partial pressure. The total concentration of the radicals reached to $1.7 \times 10^{21}\,cm^{-3}$, which is comparable to the maximum concentration of monovalent anions in the cages.

The evaluation of the radical formation enthalpy and entropy enables us determine temperature and oxygen partial pressure dependences of equilibrium oxygen radical concentration (Fig. 18). The rate-limiting process for the radical formation is not the surface reaction, but the total ionic diffusion process, in which the smallest diffusivity of O_2^- likely dominates the process. These results allow one to predict the total oxygen radical content for a given annealing condition.

3.2.3 Electron Paramagnetic Resonance of O_2^- Radicals in Cages:[62] The O_2^- ion in C12A7 was studied by continuous wave and pulsed wave EPR. A C12A7 single crystal heated in 40% ^{17}O-enriched gas showed a hyperfine splitting due to the presence of $^{17}O_2^-$. This fact clearly indicates that O_2^- is formed via reaction of an O_2 molecule in the atmosphere with an extra-framework oxide ion. The angular variations of g-values and ^{17}O hyperfine splitting were measured for the single crystal at 20 K, and also ^{27}Al-ESEEM powder patterns

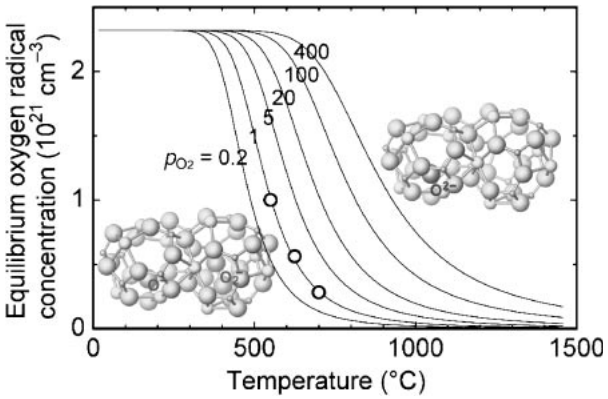

Fig. 18. Partial oxygen pressure and temperature dependences of equilibrium concentrations of oxygen radicals. Circles denote measured equilibrium concentration.

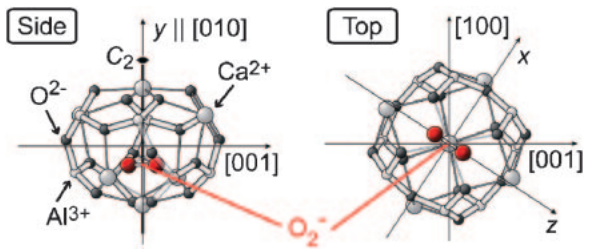

Fig. 19. Location of O_2^- inside cage in C12A7 determined by EPR study (Left: side view, Right: top view).

were measured at 4 K. These results verified that the O_2^- radical is located inside the cage, and they clarified that O_2^- is adsorbed on a Ca^{2+} ion of the lattice framework. Furthermore, the configuration of O_2^- is determined such that two constituent oxygen ions occupy crystallographically equivalent sites in the cage, indicating the O_2^- ion takes "side-on" configuration, where the O–O bond is perpendicular to the 2-hold rotation axis ($C_2 \parallel \langle 100 \rangle$) in the cage and points at the two oxide ions in the framework (Fig. 19).

Dynamics motion of the O_2^- was clarified from the temperature dependence of the *g*-values: O_2^- behaves like a solid below ~20 K, an anisotropic swinging rotation of the O–O bond along the C_2 axis is activated with temperature; and the anisotropy in the swinging motion disappears at >400 K. These results were explained in terms of the electrostatic interaction between the Ca^{2+} ion and π-orbitals of the O_2^- radical.

3.2.4 Partial Oxidation of Methane into Syngas:[63] Partial oxidation of methane into syngas (CO and H_2) was examined using C12A7 powders promoted by metals such as Ni, Co, Pt, Pd, and Ru. The effect of space velocity and metal loading was studied, and the catalytic ability of Ni/C12A7 was compared with that of a nickel catalyst supported on CaO, α-Al_2O_3, and other calcium aluminates with high CaO/Al_2O_3 ratios. On Ni, Pt, and Pd/C12A7, the reaction readily took place at temperatures as low as 500 °C and reached thermodynamic equilibrium quickly. At 800 °C and space velocity of 240000 mL g^{-1} h^{-1}, the activity of the five samples investigated decreased in the following order: 1%Pt/C12A7 > 5%Co/C12A7 > 5%Ni/C12A7 > 1%Ru/C12A7 > 1%Pd/C12A7. The activity and selectivity of Ni/C12A7 and Pt/C12A7 increased

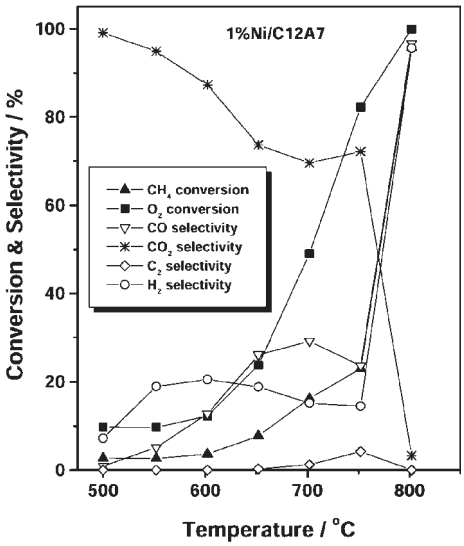

Fig. 20. CH_4 partial oxidation to syngas over 1%Ni/C12A7 as a function of temperature Gas space velocity = 30000 mL g^{-1} h^{-1}.

with metal loading, and the activity of 10%Ni/C12A7 was comparable to that of 1%Pt/C12A7. Ni/C12A7 exhibited low coke formation rate and it was more active than nickel supported on CaO, α-Al_2O_3, $3CaO \cdot Al_2O_3$, and $CaO \cdot Al_2O_3$ owing to the good dispersion of NiO on C12A7 and the existence of active oxygen ions incorporated in its nanocages (Fig. 20).

3.2.5 Generation of High-Density O^- Ion Beams:[64–67] We succeeded in extracting intense O^- ion beams by applying dc voltage to C12A7 incorporating a large amount of O^- (1.3×10^{20} cm^{-3}) and O_2^- (2.7×10^{20} cm^{-3}). The observed current was dominated by O^- ion. When the sample temperature was 800 °C and the applied electric voltage exceeds 1 kV cm^{-1}, the O^- current density was increased to ~2 μA cm^{-2}, which is higher by three orders of magnitude than the maximum value obtained from yttrium-stabilized ZrO_2 (YSZ). A surface metal electrode, essential for the YSZ to dissociate a drifting O^{2-} in the bulk into a pair of an O^- radical and an electron on the surface, is not needed for the C12A7. The presence of extremely large concentrations of O^- and O_2^- ions and the fast oxygen-ion-conductive nature of C12A7 allow for the extraction of the O^- radicals directly from the surface. The capability of generating high-density pure O^- ion current is usable for various novel oxidation processes such as the formation of gate dielectrics on semiconductors, organic chemical reactions, decomposition of pollutants, and sterilization. Development of continuous O^- beam generation system using C12A7 ceramic membrane is now in progress (Fig. 21).

3.2.6 Incorporation of H^- and Relevant Insulator–Conductor Conversion: The first electronic conduction in the main-group light metal oxides was realized in C12A7. Hydride ions (H^-) were incorporated into the cages by a thermal treatment in hydrogen atmosphere.[68] As-treated C12A7:H was colorless, transparent, and a good insulator with an electronic conductivity of less than 10^{-10} S cm^{-1}. The C12A7:H exhibited a coloration of yellowish green corresponding to optical absorptions at 2.8 and 0.4 eV with simultaneous conversion into an electronic conductor with 0.3 S cm^{-1} at 300 K upon irradiation

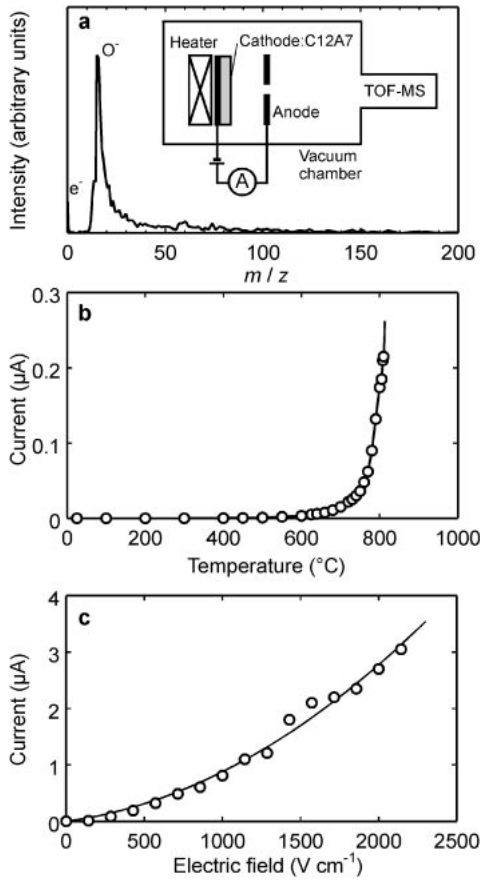

Fig. 21. (a) Typical time-of-flight type mass spectrum of ion current extracted from C12A7. (b) Ion current between two electrodes as a function of sample temperature. Extracting dc voltage was fixed at 375 V. The beam current came primarily from O^- ions. (c) Ion current from a C12A7 disk of 2 cm^{-2} area as a function of applied DC voltage at 810 °C.

of ultraviolet light (Fig. 22). The conductive state continued even after the irradiation was stopped. Reverse process or inversion to the insulator occurred when the material was heated to more than ~300 °C accompanying with a rapid decay of the optical absorption intensities. When the temperature rose above ~550 °C, H_2 gas was released from the sample and the photosensitivity was lost. By the ultraviolet light illumination, the H^- ions emit electrons to be trapped at the cages, forming F^+-like centers. Further, a migration of the electrons at the F^+-like centers is responsible for the conduction. The visible light absorption loss is estimated to be only 1% for a 200 nm thick conductive C12A7:H films. The present properties provide novel applications such as direct optical writing of conducting areas on the insulating transparent media.

Generation of persistent carrier electrons in C12A7:H by electron beam-irradiation was also examined.[69] Surface layer of an insulating single crystal were directly converted to an electronic conductor by the electron-beam irradiation, accompanied with a green coloration that has been also observed by the ultraviolet-light irradiation. Carrier electron formation at the maximum of the electron excitation was saturated by an electron beam dose of 10 μC cm^{-2}, which is comparable with

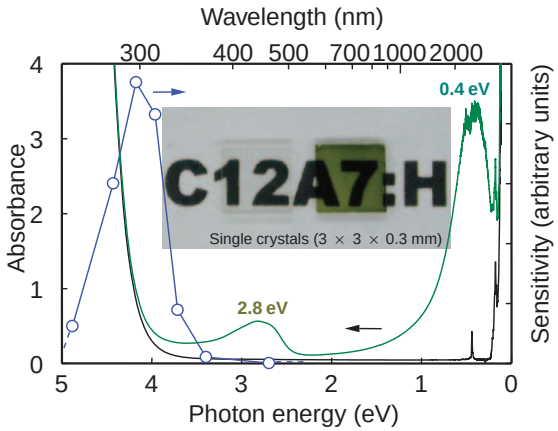

Fig. 22. Optical absorption spectra for an H^--loaded C12A7 single crystal before and after irradiation of ultraviolet light. Circles denote photon energy dependence of the sensitivity for the coloration.

the sensitivity of conventional photoresists for the electron-beam lithography. Carrier electron formation yield per an electron–hole pair was estimated to be as high as 0.05.

3.2.7 Theoretical Analysis for Electrical and Optical Properties:[70–72] An embedded cluster approach was used to study the electronic structure and optical properties of electron-containing C12A7. Our results suggested that the conduction band of the C12A7 consists of a narrow band of the empty cage states (cage conduction band) between 5.2 and 5.7 eV above the top of the valence band (VB), and the framework conduction band at about 6.7–7.0 eV above the top of the VB. The gap between the cage conduction band and the framework conduction band was estimated to be about 1 eV. The extra-electrons occupy the cage states, which split from the cage conduction band by ~4 eV above the top of VB. The electrons are localized in the cages and undergo hopping between neighboring cages. The lowest optical transition from the top of the valence band to the cage conduction band calculated using TDDFT was ~5.2 eV. The extra-framework electrons introduce two absorption bands with the experimental peaks at 0.4 and 2.8 eV. These bands were assigned to the inter-cage charge transfer and the intra-cage s–p transitions, respectively (Fig. 23). The results are useful for understanding semi-localized electron gas and strong electron–phonon coupling. They are also helpful to design new types of transparent conductors and electrides.

3.2.8 Room-Temperature Stable Electride and Field Electron Emission: An electride is a crystalline ionic salt in which electrons serve as anions. Typical examples are compounds of cryptand or crown-ether as cations and the electrons as anions.[73] Although the electrides are promising for novel applications such as a field electron emitter due to their small work functions, they are not stable at room temperature and/or in a moist atmosphere. Thus, syntheses of a stable electride have been desired for practical applications. The first thermally and chemically stable electride was realized in C12A7;[74] we eliminated the free O^{2-} ions from the cages by heating a single crystal of C12A7 in evacuated silica glass tubes together with metal calcium, leading to the formation of high-density (2×10^{21} cm^{-3}) electrons localized in the cages. The resultant

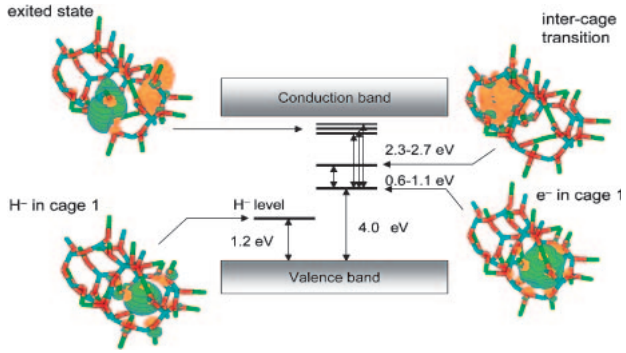

Fig. 23. Energy band diagram for C12A7 obtained by a first principle calculation based on an embedded cluster approach.

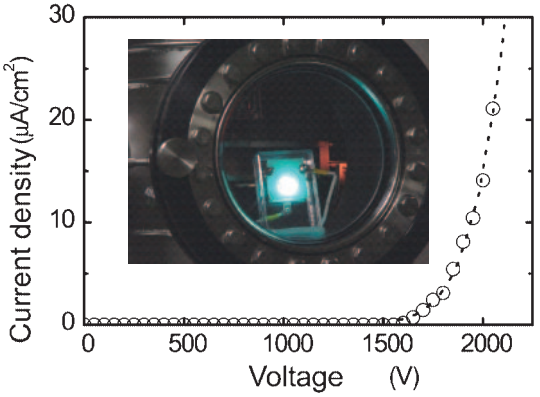

Fig. 25. Current–voltage characteristic for electron emission from single crystal C12A7 electride. Inset is a photograph of the operation of a field emission type light-emitting device using ZnO:Zn phosphor.

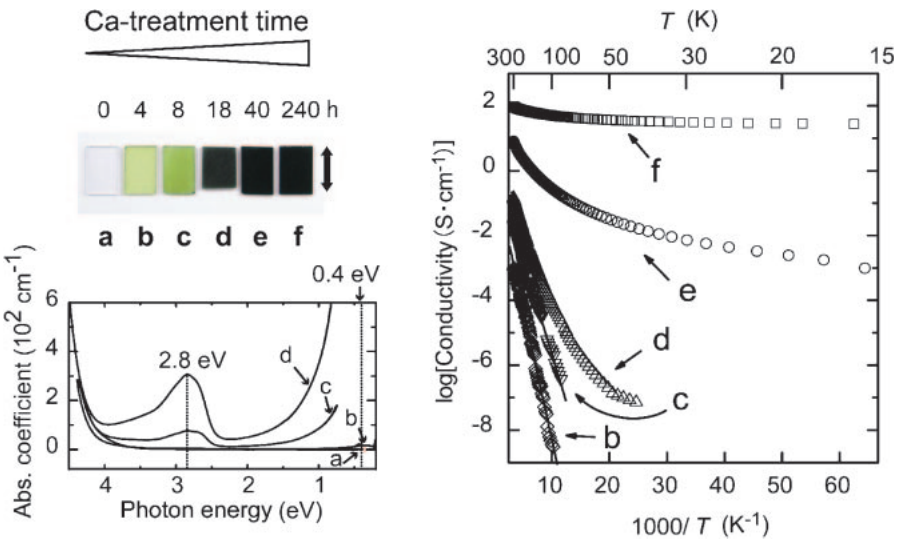

Fig. 24. Appearance of single crystals processed by the Ca-vapor annealing and their optical absorption spectra and electrical conductivity.

C12A7 is described as $[Ca_{24}Al_{28}O_{64}]^{4+}$ $(4e^-)$, i.e. C12A7 electride. The electrons localize at F^+-like centers, thereby behaving as substitution anions for free O^{2-} ions. They can migrate by hopping to neighboring cages, giving an electrical conductivity as high as $\sim 100\,S\,cm^{-1}$ (Fig. 24). Further they exhibited anti-ferromagnetic coupling, forming diamagnetic pairs or singlet bipolarons.

We investigated an electric-field electron emission from the C12A7 electride in vacuum.[75] Measured electron emission properties were understood by Fowler–Nordheim tunneling at a large electric field $>200\,kV\,cm^{-1}$ and by the thermionic emission at lower electric fields. A triode structure-device was constructed using the electride as a cathode and a ZnO:Zn phosphor plate as anode. Light emission was clearly observed under typical ambient light, demonstrating that C12A7 electride is promising for field emission display devices (Fig. 25). The work function estimated from the emission characteristics was ~ 0.6 eV, which is comparable to values reported for conventional organic electrides. However, ultraviolet photoelectron spectroscopy gave much larger value ~ 3.7 eV for the work function. The discrepancy may be attributed to the so-called band bending effect due to naturally formed n^+/n^- layers on the surface.

3.2.9 Hot Ion Implantation: We examined the formation of the H^- ions in the C12A7 films[76] by hot proton-implantation. The concentration of F^+-like centers and the electrical conductivity induced by ultraviolet light illumination, that is, the concentration of the H^- formed by the proton-implantation, increased with increasing temperature of the C12A7 film. This fact indicates that the formation of H^- is accompanied by thermal excitation processes. The optimum temperature for the H^- formation was 600–700 °C. Furthermore, the electrical conductivity after the illumination was controllable by fluences of the implanted ions. For example, fluences of $1 \times 10^{18}\,cm^{-2}$ gave electrical conductivity values as high as $\sim 10\,S\,cm^{-1}$.

Inert gas ion (Ar^+ and He^+) implantations into C12A7 films were also investigated with fluences from 1×10^{16} to $1 \times 10^{17}\,cm^{-2}$ at elevated temperatures.[77] Upon the hot implantation at 600 °C with fluences higher than $1 \times 10^{17}\,cm^{-2}$, obtained films

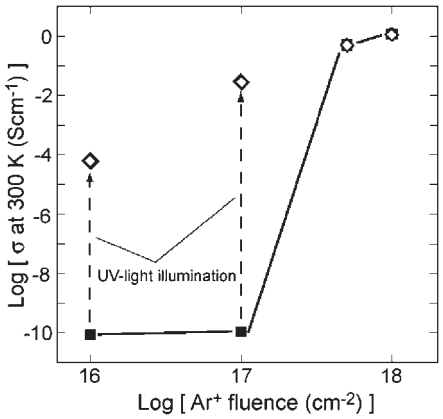

Fig. 26. Ar^+-dose dependence of electrical conductivity in C12A7 films. The symbols ■ and □ indicate electrical conductivities before and after ultraviolet-light irradiation.

were colored and exhibited electrical conductivity in the as-implanted state. It is caused by the extrusion of the free O^{2-} ions, leaving electrons in the cages at concentrations up to $\sim 1.4 \times 10^{21}\,cm^{-3}$. When the fluence is less than $1 \times 10^{17}\,cm^{-2}$, as-implanted films were transparent and insulating, and exhibited the coloration and electrical conductivity after the ultraviolet light illumination, suggesting that the H^- ions were formed by the inert gas implantation; probably preexisting OH^- ions act as precursors. The induced electron concentration was proportional to the value of dpa (displacements per atom), suggesting that nuclear collision effects of the implanted ions play a dominant role in the extrusion of the O^{2-} ions (Fig. 26). The hot ion implantation technique provides a novel non-chemical process to prepare the electron-conductive C12A7 films.

Recently, we have invented an easy and efficient synthetic method of C12A7 electride via melt without using single crystal or ion-implantation.[78] This method is suitable for massive production.

4. SiO_2 Glass for Vacuum/Deep Ultraviolet Lasers

4.1 Background and Approach. Ultraviolet (UV) light is absorbed in various materials by causing the electronic transitions from occupied to unoccupied states. The UV light of $\lambda < 200$ nm is strongly absorbed by O_2 in air but transmits efficiently in vacuum. Thus, it is called the vacuum-UV (VUV) light. The UV light of $\lambda < 300$ nm is not usually seen on the earth's surface, mainly due to the optical absorption of the ozone layer, and is sometimes called the deep-UV light. Only a limited number of dielectrics, typically oxides and fluorides of light metal cations, have enough large bandgap energies to be transparent at the DUV and VUV spectral region.

Amorphous SiO_2 (SiO_2 glass) is one of the most important DUV-VUV transparent materials. First, its UV transmission limit determined by the tail of the fundamental absorption is located at 8–9 eV,[78–82] which is the largest among the known amorphous oxides. Second, high-purity products whose metallic impurity contents are less than ~ppm or ~ppb level are commercially available. It is one benefit of the vapor-phase synthesis established in 1970s to manufacture optical telecommunication fibers and high-purity silicon ingredient obtained from the semiconductor industries. Third, as distinct features of amorphous material, SiO_2 glass is optically isotropic and has much better shape workability than crystalline materials. Fourth, SiO_2 glass has a good chemical stability, high mechanical strength, and very low thermal expansion. These properties are quite unique and useful for application to optics components.

Despite the low metallic impurity contents, the transmittance of synthetic SiO_2 glasses at DUV-VUV spectral region is often far from the theoretical limit determined by the fundamental absorption edge and the Rayleigh scattering. The main origin of this discrepancy is the structural defects embedded during their manufacturing or induced by exposure to the DUV-VUV light (Fig. 27).[83,84] The existence of these defects is very harmful for several industrial applications of SiO_2 glass. For example, they easily degrade the imaging quality of the excimer laser photolithography based on KrF ($\lambda = 248$ nm, $h\nu = 5.0$ eV), ArF (193 nm, 6.4 eV), and F_2 (157 nm, 7.9 eV) lasers where circuit patterns as fine as ~100 nm are expected to be exposed accurately. In optical fibers, the transmission loss due to the structural defects is significantly magnified because of the large optical path length. Thus, the control of the structural defects in SiO_2 glasses is a key issue to develop the optical fibers in use for the DUV-VUV region.

We focus on the studies of the DUV-VUV light-transparent SiO_2. They include the fundamental studies on structural defects and their interactions with DUV-VUV laser light, and developments of SiO_2 glasses for excimer laser photolithography and of optical fibers transmitting ArF-laser light. Chemical disorder, i.e., structural defects, has been primarily studied over the last 2 decades. As a consequence, the quality of silica has much improved and structural defects are no longer a primary issue in this decade. In this study, emphases were placed on physical disorder, i.e., strained chemical bonds, and role of interstitial gas molecules which may accommodate in silica.

4.2 Research Topics. 4.2.1 Effects of Physical Disorder on VUV Transparency: 4.2.1.1 Physical Disorder in SiO_2 Glass; The three-dimensional network of corner-shared SiO_4 tetrahedra is a common description of most of the crystalline and amorphous SiO_2 polymorphs. In crystalline SiO_2, the SiO_4 tetrahedra are arranged regularly. For example, in α-quartz, whose optical properties have been studied intensively, all the tetrahedra are equivalent and all the Si–O–Si bonds have the same bridging angle (~144°). Thus, the distortion of the lattice is minimized. On the other hand, the SiO_4 tetrahedra are randomly arranged in amorphous SiO_2 (SiO_2 glass). However, the local structure of SiO_2 glass is distorted to maintain the disordered three-dimensional network. In general, such distortion is maximized at the flexible parts of the structure. The observations by various techniques indicate that the structural strain in SiO_2 glass is relaxed mainly by changing the internal and torsional (dihedral) angles of the Si–O–Si bonds while maintaining the Si–O bonding length and the O–Si–O angle almost constant. Thus, the Si–O–Si angle in SiO_2 glass is largely scattered and the scattering, which can be referred as the "physical disorder," inherently distinguishes amorphous SiO_2 from crystalline forms. The strain energy per Si–O–Si bond increases as the angle θ deviates from the most stable geometry ($\theta = 140$–$150°$). One of the typical strained bonds in SiO_2

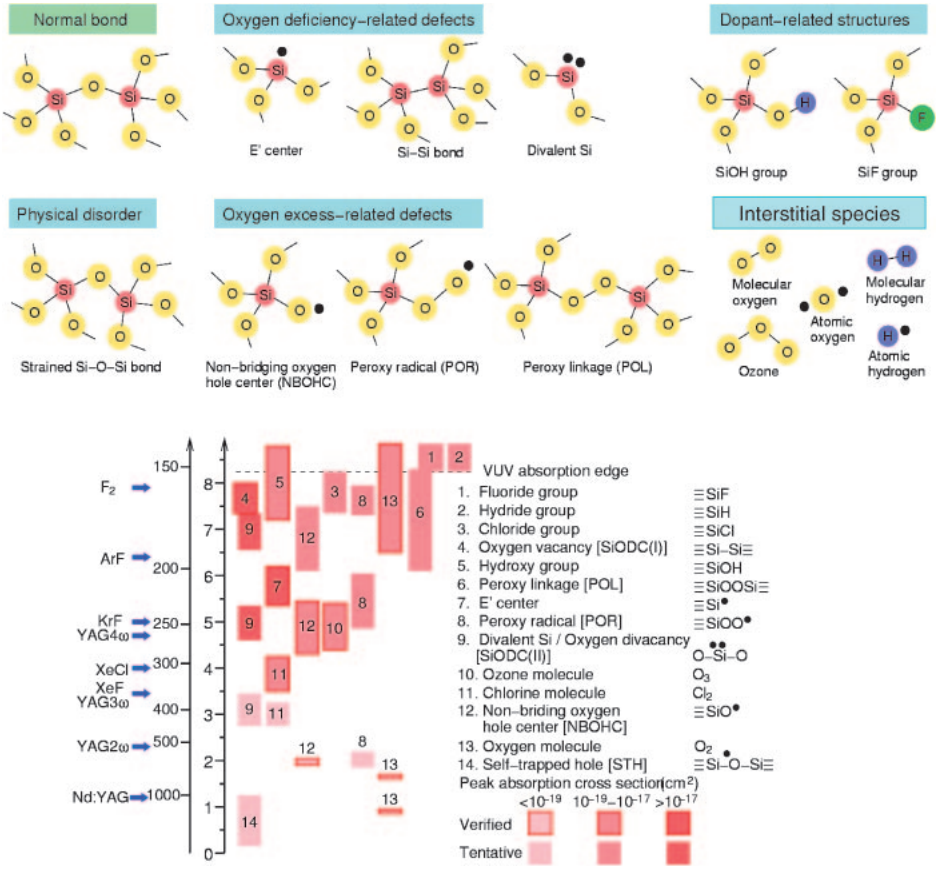

Fig. 27. Optical absorption bands and configurations of principal structural defects in SiO_2 glass.[82] Light wavelengths of various lasers are also shown.

glass is a Si–O–Si bond consisting of the three-membered ring ($\theta \sim 130°$), which can be monitored by the Raman band at 606 cm^{-1}.[85]

Several observations have suggested that VUV transparency of SiO_2 depends on the Si–O–Si angle. In densified SiO_2 glass, the average Si–O–Si angle decreases[85] and the fundamental absorption edge shifts to the lower energy side.[86] The band-gap energy of SiO_2 glass is smaller than that of α-quartz.[87] Thus, it is important to modify the degree of the disorder of SiO_2 glass for improving the transparency of SiO_2 glass near the fundamental absorption edge.

Transmittance and toughness against F_2-laser light were examined for SiO_2 glass samples with different distributions of the Si–O–Si angles.[88,89] Our study was implemented by changing the glass structure in equilibrium with a fixed temperature. This was achieved by thermal annealing at different temperatures (referred as T_f hereafter). Both the optical absorption near the fundamental edge of SiO_2 glass (Fig. 28) and the optical absorption induced by the exposure to F_2 laser (~2.5 mJ cm^{-2}, 8.4×10^6 pulses) (Fig. 28, inset) increase with an increase in T_f. Color centers dominating the laser-induced absorption bands are the E' center (a silicon dangling bond, ≡Si•, 5.8 eV) and the non-bridging oxygen hole center (NBOHC, an oxygen dangling bond, ≡SiO•, 4.8 and 6.8 eV).

Since comparable concentrations of the E' centers and NBOHC are formed, photo-decomposition of the strained Si–O–Si bond (Fig. 28) is suggested to dominate the defect

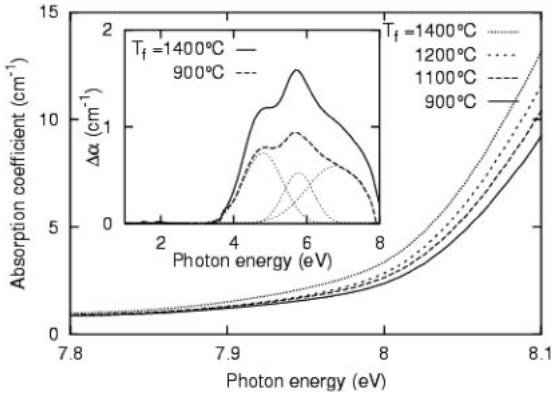

Fig. 28. VUV optical absorption spectra of SiO_2 glasses with different T_f values. The inset shows the F_2-laser-induced optical absorption spectra for $T_f = 900$ and 1400 °C samples.

formation processes, i.e., ≡Si–O–Si≡ ⇌ ≡Si–O• + ≡Si•.

Next, defect formation was examined as a function of pulse energy of F_2 laser.[90–92] At <10 mJ cm^{-2}, the concentrations of the laser-induced defects increase linearly with the pulse energy, indicating that the one-photon absorption process controls the defect formation (Fig. 29). However, above this threshold energy, the concentrations of the laser-induced defects enhance proportionally with the pulse energy squared. This quadratic power dependence is similar to that commonly seen for the

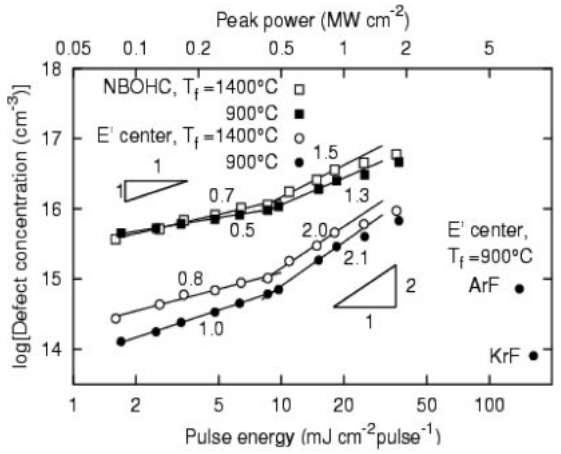

Fig. 29. Concentrations of the E' center and NBOHC as a function of the pulse energy of F_2, ArF, or KrF laser. Samples were exposed to 3×10^4 laser pulses to create the defects.

KrF- or ArF-laser-induced defect processes via the two-photon absorption process, while this defect process is distinctively different from the ones observed because the quantum yield of the F_2-laser-induced defects is ~3 orders of magnitude larger than that of the KrF- or ArF-laser-induced defects. In contrast to the case of the KrF- and ArF-laser light, F_2-laser light directly excites the weak absorption tail near the fundamental absorption edge, typically consisting of the strained Si–O–Si bonds and the SiOH groups. The two-step absorption of F_2-laser photons via such real intermediate states is the probable mechanism for the efficient defect formation by the F_2-laser irradiation. Therefore, it is crucial to suppress the weak absorption tail for improving the radiation toughness of SiO_2 glass to the F_2-laser light.

4.2.1.2 Reduction of Physical Disorder by Terminal Functional Groups; Figures 28 and 29 indicate that the strained Si–O–Si bond is the dominant factor controlling the transmittance near the fundamental absorption edge. One of the possible measures to reduce the strained Si–O–Si bonds is to relax the glass structure by a low-temperature thermal annealing. However, this has a drawback that the structural relaxation time increases very quickly with increasing T_f because of the large activation energy of the viscous flow of SiO_2 glass (~5–7 eV). An alternative approach is the acceleration of the structural relaxation by reducing the viscosity. This can be performed by breaking up the glass network with incorporating terminal functional groups such as the SiOH and SiCl groups. For example, SiO_2 glasses containing SiOH groups (wet SiO_2 glass) exhibit a good KrF- and ArF-laser toughness because of the reduction of the strained bonds.

4.2.2 Mobile Interstitial Hydrogen: 4.2.2.1 In-Situ Observations of Mobile Hydrogen Atoms and Molecules; The silanol (SiOH) group is one of the most important absorbers of the F_2-laser light in the synthetic SiO_2 glass.[93] Interactions of the SiOH groups with F_2-laser photons were investigated using the concentration change of photolysis product of the SiOH groups, the oxygen dangling bonds (termed "non-bridging oxygen hole centers," NBOHC, ≡SiO•). The photoluminescence of NBOHC at 1.9 eV was excited with frequency-quadruplicated Nd:YAG laser pulses which were synchronized with the F_2-laser pulses, and detected in-situ to record the concentration change of NBOHCs soon after (~100 μs) their creation.

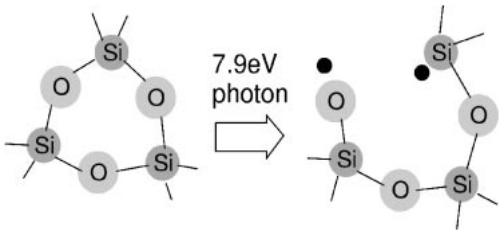

Fig. 30. Schematic illustration of photolysis of strained Si–O–Si bond.

In wet SiO_2 glass containing ~10^{20} cm^{-3} of the SiOH groups, a large amount of NBOHC is formed even with exposure to a single F_2-laser pulse. It is followed by a rapid reduction of the NBOHC concentration within one second and subsequent gradual decrease. On the other hand, the formation of NBOHC in dry SiO_2 glass (SiOH $<10^{17}$ cm^{-3}) due to the dissociation of the Si–O–Si bonds becomes detectable only after the exposure of more than ~10 F_2-laser pulses. The quantum yield for the wet SiO_2 glass is ~0.1, which is far larger than that for the dry SiO_2 glass, ~10^{-4}, indicating that the F_2-laser photolysis of the SiO–H bond is remarkably efficient.

A result to be noted is that the decay of F_2-laser-induced H^0 appears even in the sample whose H_2 content is below the detection limit before the F_2-laser irradiation. This observation demonstrates that the formation of H_2 due to the dimerization of H^0 occurs.[94] In the H_2-loaded sample, NBOHC does not remain at 300 K, clearly showing that H_2 is very mobile in SiO_2 glass at ambient temperature.

4.2.2.2 Effects of Mobile Hydrogen Species on Defect Formation and Annihilation; The effects of mobile hydrogenous species on defect formation and annihilation processes are not simple. The observations in the previous section indicate an important role of mobile interstitial H^0 and H_2 in annihilation of the dangling-bond type defects such as NBOHC and the E' center. This effect is clearly seen by comparing the formation and decay of NBOHC in H_2-free and H_2-loaded samples exposed to F_2-laser pulses at ambient temperature (Fig. 30).[94]

Irradiation with an F_2-laser pulse creates nearly the same concentrations of NBOHC in both the H_2-free and the H_2-loaded samples, indicating that the interstitial H_2 does not influence the quantum yield of the formation of NBOHC. However, in the H_2-loaded sample, NBOHC disappears quickly and does not accumulate due to the recombination with H_2.

In contrast, the interstitial H_2 accelerates the laser-induced formation of the Si–Si bonds (Fig. 31).[95] In H_2-free samples, both the ArF- and the F_2-laser irradiations induce optical absorption bands dominated by the E' center and NBOHC at DUV-VUV spectral region. In the H_2-loaded sample, in contrast, the optical absorption bands due to the E' center and NBOHC are largely destroyed because of their conversions into the SiH and SiOH groups, while the 7.6 eV absorption band of the Si–Si bonds is induced. This phenomenon can be regarded as the photochemical reduction of the glass network with H_2. The degradation of the 7.9 eV transmittance of the H_2-loaded sample compared to that of the H_2-free sam-

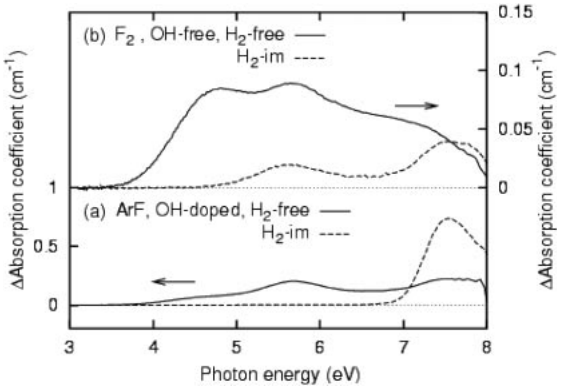

Fig. 31. Effects of interstitial H_2 on change of optical absorption spectra in SiO_2 glasses exposed to (a) ArF-laser light, and (b) F_2-laser light.

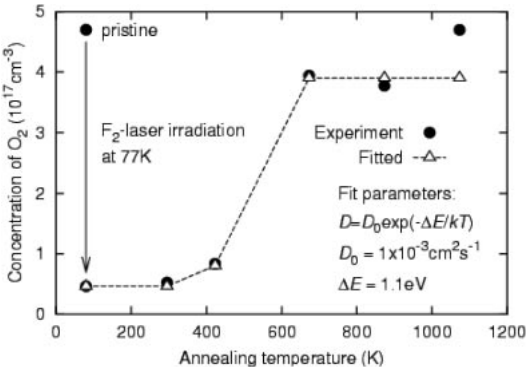

Fig. 32. Concentration change of O_2 in O_2-rich SiO_2 glass exposed to F_2-laser light at 77 K and subsequently annealed at 15 min at each temperature designated.

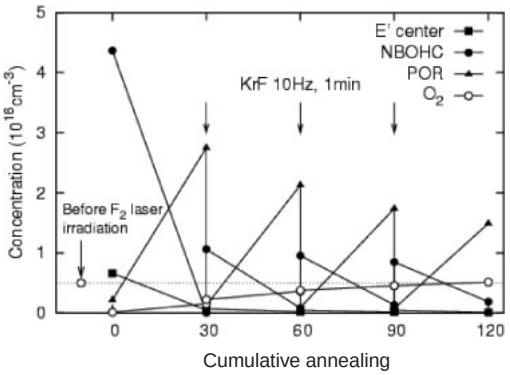

Fig. 33. Concentration changes of the E' center, NBOHC, POR, and interstitial O_2 in the F_2-laser-irradiated high-O_2 sample during multiple cycles of thermal annealing (30 min at 500 °C) and subsequent brief exposure to KrF-laser light at ambient temperature (600 pulses of ~100 mJ cm^{-2} pulse^{-1}). The dotted line indicates the O_2 concentration before the F_2-laser irradiation.

ple leads to a conclusion that H_2 loading is not suitable for SiO_2 glasses used with F_2 lasers. This finding is rather important for practical applications.

Another noticeable effect of the interstitial H_2 is the laser-induced crack formation.[96] The photochemical reduction of SiO_2 glass with H_2 creates a lot of crack propagation by water, which was studied well and the commonly termed "stress corrosion."[97] Thus, it is plausible that the photo-reduction of the glass network with H_2 enhances the crack formation by the stress corrosion mechanism.

These trade-offs insist that the concentration of H_2 should be optimized depending on the photon energy and pulse energy of light sources.

4.2.3 Mobile Interstitial Oxygen Species in SiO_2 Glass: 4.2.3.1 Diffusion and Photochemical Reactions of Oxygen Atoms; The Frenkel defect involving a pair constitution of a vacant lattice site and an interstitial atom is one of the most fundamental defects in solids. The Frenkel defect in SiO_2 glass is a pair of the oxygen vacancy (the Si–Si bond) and the interstitial oxygen atom (O^0). They are created by dense electronic excitation of SiO_2 glass with ArF-laser light, X-rays, proton, neutron, and electron beams.[98–100] The Si–Si bond and phenomena involving its formation and destruction have been extensively studied because it is detectable by an optical absorption band at 7.6 eV and photoluminescence bands at 2.7 and 4.4 eV. However, the properties of O^0 largely remain uncertain. This is primarily because of the lack of distinct spectroscopic signatures of O^0.

One possible way to examine the properties of O^0 is to selectively create O^0 in SiO_2 glass. The F_2-laser light directly excites the dissociative Schumann–Runge band of O_2 appearing at >6.5 eV[101] and efficiently photolyzes it into a pair of O^0. Thus, a measurable amount of O^0 can be created in SiO_2 glass by exposing the SiO_2 glass containing the interstitial oxygen molecules (O_2) to the F_2-laser light. Concentration changes of O_2 were monitored by photoluminescence of O_2 at 1272 nm excited at 1064 nm using a Nd:YAG laser.[102] A brief exposure of an O_2-rich SiO_2 glass to the ArF- or F_2-laser light creates the interstitial ozone molecules (O_3) due to the addition of a photo-generated O^0 to a remaining O_2.[103] A long-time exposure to the F_2-laser light largely destroys these poly-oxygen species, simultaneously inducing an optical absorption band at ~7.1 eV with an oscillator strength of ~0.01.[104] The photo-generated O^0 shows a large thermal stability: It is immobile at ambient temperature and starts to migrate at ~200–400 °C. The thermal recovery of O_2 due to the recombination of the O^0 atoms allows estimating the diffusion coefficient and the activation energy of the diffusion of O^0 (Fig. 32). These observed properties of O^0 agree well with theoretical predictions indicating that O^0 should take the form of the peroxy linkage (≡Si–O–O–Si≡).[105–107]

Reactions of O^0 with paramagnetic centers sensitively detected by EPR can be another way to monitor O^0. Addition of O^0 to NBOHC to form the peroxy radical (POR, ≡SiOO•), which has not been verified experimentally, could be a possible probe reaction. A simultaneous F_2-laser photolysis of O_2 and the SiOH groups prepares samples suitable for this purpose, i.e. samples containing O^0 and NBOHC as dominant chemical species. Thermal annealing of the sample at 500 °C destroys NBOHC with increasing the concentration of POR, verifying that the conversion of NBOHC into POR efficiently occurs. In addition, this reaction is reversed by dissociating the O–O bond of POR[108] with photo-exciting its optical absorption at ~5 eV (Fig. 33). These studies demonstrate that O^0 plays an

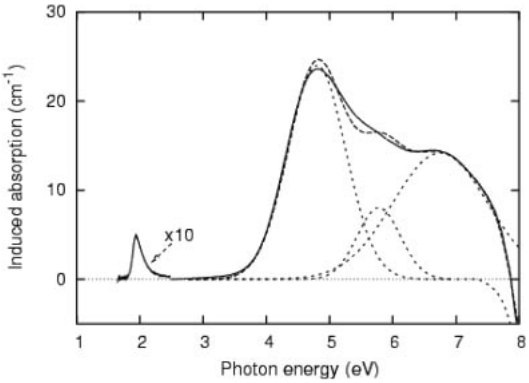

Fig. 34. Induced optical absorption spectrum for wet SiO_2 glass exposed to F_2-laser light below 95 K. The spectrum at >3 eV is fitted with optical absorption bands of NBOHC (4.8 and 6.8 eV), E' center (5.8 eV), and SiOH groups (>7.4 eV) (dotted lines).

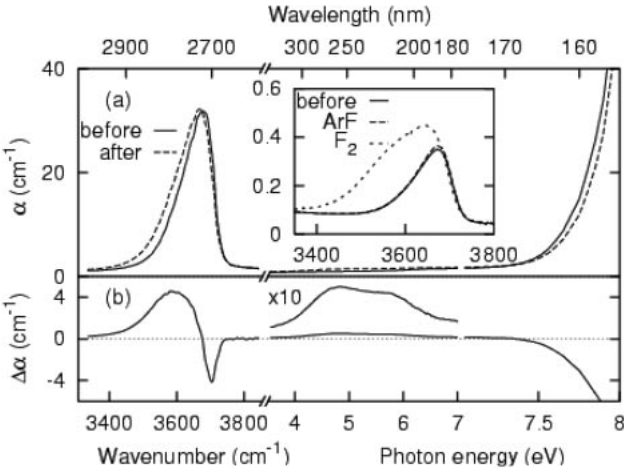

Fig. 35. Changes in optical absorption spectra of silica glass with exposure to F_2-laser light. The inset shows the change in IR absorption spectra of SiOH band with exposure to ArF- or F_2-laser light.

important role in the defect processes in the SiO_2 glass.

4.2.4 Optical Properties of Several Network-Bound Structural Defects: 4.2.4.1 VUV Absorption Band of NBOHC; The oxygen dangling-bond (termed as "non-bridging oxygen hole center," ≡SiO•) is one of the fundamental defects in SiO_2 glasses. Although it has been established that NBOHC has optical absorption bands at 1.97 and 4.8 eV,[109] VUV absorption of NBOHC has not been identified, probably because optical absorption bands attributable to various structural defects significantly overlap at this spectral region.

To distinguish the absorption bands of NBOHC from other interference absorptions, we used a large amount of NBOHC ($>10^{18}$ cm^{-3}) that was created by photo-decomposing the SiOH groups with the F_2-laser light below 95 K; the thermal annihilation of the induced absorption bands was measured.[110] The induced optical absorption at DUV-VUV spectral region consists of three Gaussian-shaped bands, one of them centered at 4.8, at 5.8, and at 6.8 eV (Fig. 34).

The 4.8 and 5.8 eV bands originate from NBOHC and the E' center, respectively. The intensity of the 6.8 eV band changes simultaneously with that of the 4.8 eV band, which indicates that the 6.8 eV band is also assigned to NBOHC. This assignment is further supported by the observation that excitations at 4.7 and 6.4 eV give the 1.9 eV photoluminescence with the same spectral shape and decay constant as those of the luminescence of NBOHC. A theoretical calculation indicates that the 4.8 and 6.8 eV bands of NBOHC are both due to the transition from the 2p non-bonding state of the bridging oxygen ions to the half-filled 2p orbital on the dangling oxygen atom.[111] Very recently, the presence of the 6.8 eV band has been verified by a photoluminescence excitation experiment.[112]

4.2.4.2 Photo-Structural Change of the SiOH Groups; Optical absorption due to the SiOH group resides at >7.4 eV. Direct excitation of this optical absorption band with the F_2-laser light was found to shift the infrared absorption band of the SiOH groups at 3700 cm^{-1} to the lower energy side via the one-photon absorption process, accompanied by a blue shift of the VUV optical absorption band of the SiOH group (Fig. 35).[113,114] This finding indicates that the bonding configuration of the SiOH groups alters from the isolated to the hydrogen-bonded states with the exposure to the F_2-laser light.

Another distinct feature of the F_2-laser-induced hydrogen-bonded state is its high thermal stability. That is, the hydrogen-bonded state is stable at ambient temperature and its thermal relaxation becomes measurable only above ~300 °C. The activation barrier of the thermal relaxation is ~1.7 eV, which is much larger than that (~0.1 eV) of the hydrogen-bonded state thermally induced by cooling. It is very likely that a certain kind of photo-structural change extending around the SiOH group is responsible for the exceptional stability of the SiOH group in the F_2-laser-induced hydrogen-bonded state. It is noteworthy that the similar photo-induced hydrogen-bonded state is formed with the exposure to Xe excimer lamp light. On the other hand, a similar state is not formed with the exposure to ArF-laser light. Thus, the formation of the photo-induced hydrogen-bonded state does not relate to the volume compaction induced by the two-photon absorption of ArF-laser photons.

4.2.5 Development of DUV-VUV Transparent SiO_2 Glass Devices: 4.2.5.1 Optical Components for F_2-Laser Photolithography; Most of the synthetic SiO_2 glasses prepared so far are classified into the wet and dry types. The dry SiO_2 glass, commonly referred as "Type IV," have been developed with the clear purpose of the application to optical fibers for telecommunication with maximizing the transmittance at around ~1.5 μm, which has been realized by reducing metallic impurities and SiOH contents. However, it often contains the SiCl groups, the interstitial O_2, and the Si–Si bonds, all of which do not influence the infrared transmittance. On the other hand, the wet SiO_2 glass referred as "Type III" contains a considerable amount of the SiOH groups, as much as ~10^{20} cm^{-3}. It is widely used as optical material for UV-DUV lasers because the SiOH groups do not absorb the UV-DUV light and the strained Si–O–Si bonds are largely removed due to the relatively low viscosity, resulting in good radiation toughness. However, it has been difficult to simultaneously remove all of the centers absorbing F_2-laser light, such as the strained Si–O–Si bond, the Si–Si bond and the SiOH group. Figure 36

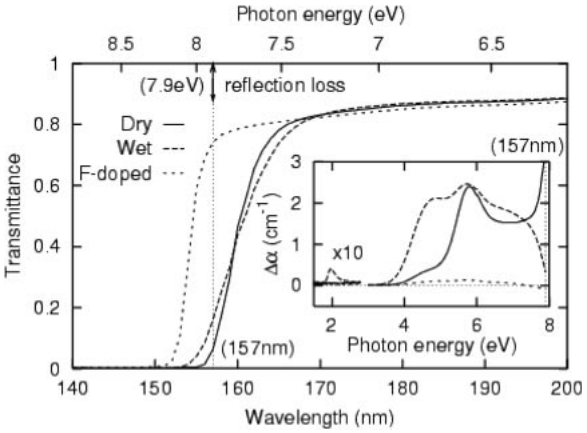

Fig. 36. Optical transmission spectra of various types of synthetic SiO_2 glass. Sample thickness = 1.0 mm. Inset is absorption induced by F_2-laser irradiation.[6]

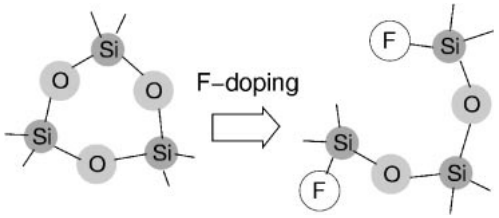

Fig. 37. Schematic illustration of structural change due to fluorine-doping. F-doping removes the small ring structures with high strain via reaction.

summarizes VUV-UV transmission spectra of various kinds of synthetic SiO_2 glasses.[115,116]

This deadlock has been eliminated by the fluorine-doping. Similar to the case of the SiOH and SiCl groups, the incorporation of the SiF groups enhances the structural relaxation and reduces the strained Si–O–Si bonds (Fig. 37). However, the SiF group is different from the SiOH and SiCl groups in that the SiF group does not exhibit optical absorption within the bandgap of SiO_2 glass. Further, the Si–F bond is difficult to photolyze because of its large bonding energy, much larger than that of the Si–O bond. Figure 36 demonstrates that the fluorine-doped SiO_2 glass exhibits the good transmittance and radiation toughness to F_2-laser light. The fluorine-doped SiO_2 glass, often referred as "*Modified Silica Glass*," meets the requirements for the photo-mask substrates in the F_2-laser photolithography.

4.2.5.2 Deep-UV Optical Fiber; Optical fibers transmitting the DUV-VUV light is an attractive device that allows deliver of DUV-VUV light avoiding the transmission loss due to oxygen molecules in air. Although a good UV-VUV transparency and shape workability of SiO_2 glass are suitable for developing such fibers, actual production of the DUV-VUV fiber is not easy because of the following reasons. First, the long optical path length requires reducing the color centers to the level much lower than that needed for the bulk glass applications. Second, a part of dangling bonds, which are inevitably created by the deformation during the fiber drawing process, often remains in the resultant fibers as the drawing-induced defects.[117] Third, as a result of the quenching from ~2000 °C,

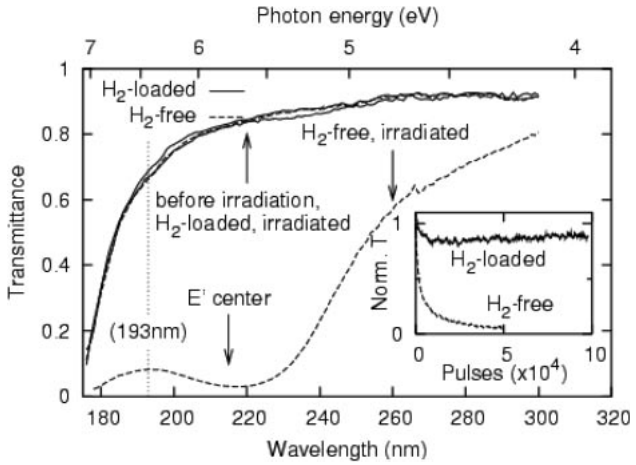

Fig. 38. Transmittance of 1 m H_2-free and H_2-loaded deep-UV fibers before and after exposure to ArF-laser pulses. The inset shows the change of normalized ArF-laser transmittance as a function of the number of ArF-laser pulses.

the fiber contains a relatively large number of the strained Si–O–Si bonds and defect precursors, which potentially turn to color centers with the exposure to the UV-VUV light. These problems have been partly overcome by incorporating SiOH groups to enhance the structural relaxation,[118] while the transmittance and radiation toughness at <200 nm have not been satisfactory.[119,120]

Studies described in the previous sections indicate that fluorine-doping is a possible way to reduce the color centers and their precursors in the fiber. Optical fibers doped by the SiF group both in the core and clad part were prepared.[120] The difference of the refractive index was built in by incorporating more SiF groups into the clad part than that in the core part. Although the initial transmittance of a meter long fluorine-doped fiber for the ArF-laser light is as high as ~60%, the transmittance decreases rapidly during the ArF-laser irradiation because of the formation of the E' centers. However, the H_2 loading avoids the accumulation of the E' centers and largely improves the radiation toughness (Fig. 38). As a result, the transmittance of the H_2-loaded fiber remains almost constant during the exposure to ArF laser up to $\sim 10^5$ pulses at ~50 mJ cm^{-2}. An additional benefit of this fiber is that the fiber tip can be easily sharpened by an immersion of the fiber into hydrofluoric acid.[121] This feature is useful for the application of the fiber as an optical probe tip for deep-UV SNOM. The patent of these DUV fibers has been licensed and various types of fibers (Fig. 39) are now commercially available.

5. Future Prospects

Figure 40 summarizes the current status of transparent oxide semiconductors (TOSs) which we have cultivated to date. The world of TOS was opened by our discovery of p-type transparent conductive oxide in 1997. A totally unexpected and very exciting result was the finding of persistent electronic conductivity in C12A7, which was widely believed as a representative insulator as listed in textbooks.

The huge potential of oxides has appeared when the high T_c-superconducting oxide was discovered in 1986. Since then, many researchers have focused on the electronic nature of

transition-metal oxides and this excitement is cultivating a new research field: so-called strongly electron-correlated oxides. However, transparent oxides, which are primarily composed of abundant light metal elements, have not been considered as a platform for electron active materials. From the view point of resource and environment issues this is just desirable direction of material search for realizing novel functionality or high performance, utilizing abundant elements as ingredients. We'd like to call this a "*ubiquitous element strategy*." Our research on C12A7 described in section **3** may be regarded as a successful case study, demonstrating the importance and power of build-in nanostructure in an apparently boring material. A combination of appropriate choice of nanostructure embedded in the materials combined with good quality of the sample with a proper shape (single crystal or epitaxial thin film) will be a key to success of the material research aiming at such an ubiquitous element strategy.

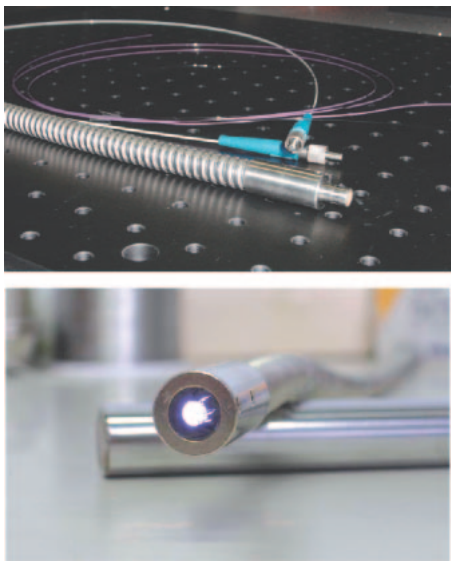

Fig. 39. Photo of DUV-fiber bundle.

As for extension of transparent oxide semiconductors, research activity is rapidly growing in our country as well as foreign countries, i.e., the U.S.A., Europe, and Asia for transparent electronics as the next generation of electronics. There are several factors working for acceleration of research activity in this field. One is the continuing increase of demand for ITO because it is needed as a transparent electrode material for each display and solar cell. The price of ITO is increasing by an order of magnitude over the past 3-year period. Exploration of novel TCO as ITO alternative is an emerging issue to be resolved by innovative material research. Another factor is the high expectations of UV-LED based on ZnO. Although UV-LED based on GaN is now well established, it is expected that ZnO LED has some advantages in various respects including material cost over GaN. The last, but not least, factor is potential application of amorphous transparent oxide semiconductors to rapidly growing flexible electronics.[122] Shifts of large area electronics on glass substrate to plastics is an undoubted trend. Thin film transistors (TFT), an elemental building block for switching devices, are needed to be fabricated on plastics in place of glasses. As a consequence, low temperature deposition of TFT is an essential requirement for channel materials. So far, organic semiconductors have been extensively studied for this application. Recently, we reported that room temperature-fabricated FET on PET films using a transparent amorphous oxide semiconductor $InGaZnO_3$ exhibits high field effect mobility of $\sim 10\,cm^2\,V^{-1}\,s^{-1}$, which is higher by an order of magnitude than that in amorphous hydrogenated Si and in pentacene.[123] This material, found following our chemical design concept,[124,125] is so chemically stable that passivation is not required. This discovery is attracting attention to amorphous transparent oxide semiconductors[126–129] which has not focused.

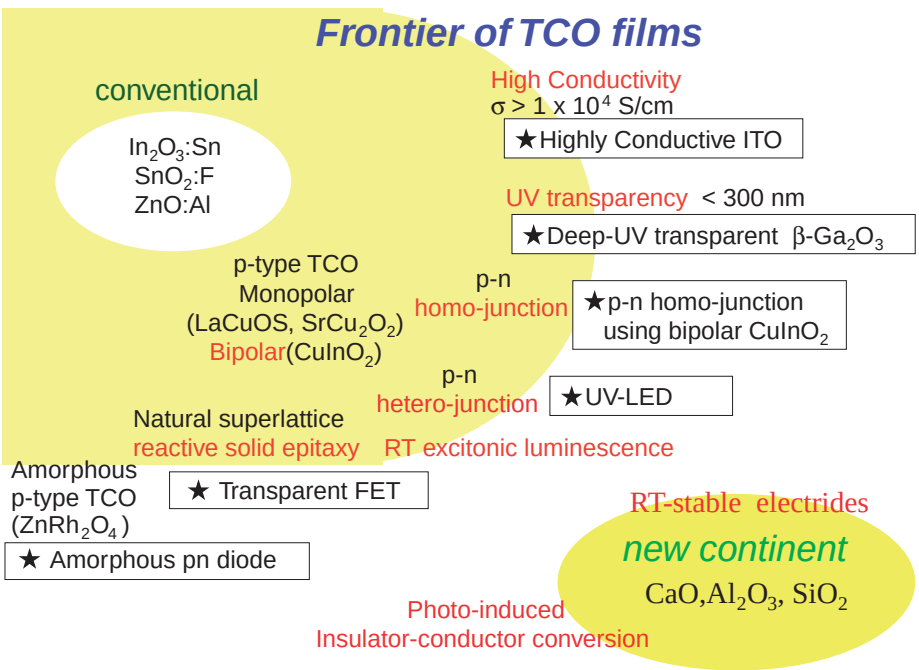

Fig. 40. Current status of transparent oxide semiconductors.

We hope that truly innovative research will cultivate a new frontier of transparent oxides as an electro-active material and lead to the realization of a sustainable society.

The study described here was primarily performed in the period from 1999 to 2004 at Materials and Structures Laboratory, Tokyo Institute of Technology and Hosono Transparent Electro-active Materials Projects, an ERATO Project, sponsored by Japan Science and Technology Agency with many collaborators. The authors express their sincere thank to Drs. Hiromichi OHTA, Masahiro ORITA, Hidenori HIRAMATSU, Kenji NOMURA, Kazushige UEDA, Hiroshi YANAGI, Katsuro HAYASHI, Masashi MIYAKAWA, Satoru MATSUISHI, Hayato KAMIOKA, Satoru NARUSHIMA, Kouichi KAJIHARA, Yoshiyuki IKUTA, Masanori OTO, Peter SUSHKO, Alexander SHLUGER, Linards SKUJA, and other graduate students of our laboratory. One of the authors (HH) expresses his sincere thank to Professor Emeritus of Tokyo Tech. Hiroshi KAWAZOE, for his guidance through extensive cooperative work to this fertile but uncultivated research area.

References

1 H. Kawazoe, M. Yasukawa, H. Hyodo, M. Kurita, H. Yanagi, H. Hosono, *Nature* **1997**, *389*, 939.

2 H. Kawazoe, H. Yanagi, K. Ueda, H. Hosono, *MRS Bull.* **2000**, *25*, 28.

3 H. Hosono, M. Yasukawa, H. Kawazoe, *J. Non-Cryst. Solids* **1996**, *203*, 334.

4 T. Gordon, *Nature* **1997**, *389*, 907.

5 H. Hosono, J. Nishii, *Opt. Lett.* **1999**, *24*, 1352.

6 H. Hosono, M. Mizuguchi, L. Skuja, T. Ogawa, *Opt. Lett.* **1999**, *24*, 1549.

7 M. Mizuguchi, H. Hosono, H. Kawazoe, *J. Opt. Soc. Am. B* **1999**, *16*, 1153.

8 N. Itoh, M. Stoneham, *Materials Modification by Electronic Excitation*, Cambridge University Press, Cambridge, **2001**.

9 K. Ueda, T. Hase, H. Yanagi, H. Kawazoe, H. Hosono, H. Ohta, M. Orita, M. Hirano, *J. Appl. Phys.* **2001**, *87*, 1790.

10 A. Kudo, H. Yanagi, H. Hosono, H. Kawazoe, *Appl. Phys. Lett.* **1998**, *73*, 220.

11 H. Ohta, M. Orita, M. Hirano, I. Yagi, K. Ueda, H. Hosono, *J. Appl. Phys.* **2002**, *91*, 3074.

12 H. Mizoguchi, M. Hirano, S. Fujitsu, T. Takeuchi, K. Ueda, H. Hosono, *Appl. Phys. Lett.* **2002**, *80*, 1207.

13 N. Ueda, H. Hosono, R. Waseda, H. Kawazoe, *Appl. Phys. Lett.* **1997**, *70*, 3561.

14 M. Orita, H. Ohta, M. Hirano, H. Hosono, *Appl. Phys. Lett.* **2001**, *77*, 4166.

15 M. Orita, H. Hiramatsu, H. Ohta, M. Hirano, H. Hosono, *Thin Solid Films* **2002**, *411*, 134.

16 H. Mizoguchi, M. Orita, M. Hirano, S. Fujitsu, T. Takeuchi, H. Hosono, *Appl. Phys. Lett.* **2002**, *80*, 4732.

17 K. Shimakawa, S. Narushima, H. Hosono, H. Kawazoe, *Philos. Mag. Lett.* **1999**, *79*, 755.

18 S. Narushima, M. Orita, M. Hirano, H. Hosono, *Phys. Rev. B* **2002**, *66*, 035203.

19 M. Orita, H. Ohta, M. Hirano, S. Narushima, H. Hosono, *Philos. Mag. B* **2001**, *81*, 501.

20 S. Narushima, H. Mizoguchi, K. Simizu, K. Ueda, H. Ohta, M. Hirano, T. Kamiya, H. Hosono, *Adv. Mater.* **2003**, *15*, 1409.

21 H. Ohta, M. Orita, M. Hirano, H. Tanji, H. Kawazoe, H. Hosono, *Appl. Phys. Lett.* **2000**, *76*, 2740.

22 H. Ohta, M. Orita, M. Hirano, H. Hosono, *Appl. Phys. Lett.* **2002**, *91*, 3547.

23 H. Ohta, H. Mizoguchi, M. Hirano, S. Narushima, T. Kamiya, H. Hosono, *Appl. Phys. Lett.* **2003**, *82*, 823.

24 H. Yanagi, K. Ueda, H. Hosono, H. Ohta, M. Orita, M. Hirano, *Solid State Commun.* **2002**, *121*, 15.

25 H. Ohta, K. Kawamura, M. Orita, M. Hirano, N. Sarukura, H. Hosono, *Appl. Phys. Lett.* **2000**, *77*, 475.

26 H. Ohta, M. Hirano, K. Nakahara, H. Maruta, T. Tanabe, M. Kamiya, T. Kamiya, H. Hosono, *Appl. Phys. Lett.* **2003**, *83*, 1029.

27 H. Ohta, T. Kambayashi, M. Hirano, H. Hoshi, K. Ishikawa, H. Takezoe, H. Hosono, *Adv. Mater.* **2003**, *15*, 1258.

28 H. Ohta, T. Kambayashi, K. Nomura, M. Hirano, K. Ishikawa, H. Takezoe, H. Hosono, *Adv. Mater.* **2004**, *16*, 312.

29 H. Ohta, K. Nomura, M. Orita, M. Hirano, K. Ueda, T. Suzuki, Y. Ikuhara, H. Hosono, *Adv. Funct. Mater.* **2003**, *13*, 139.

30 K. Ueda, S. Inoue, S. Hirose, H. Kawazoe, H. Hosono, *Appl. Phys. Lett.* **2000**, *77*, 2701.

31 K. Ueda, S. Inoue, H. Hosono, N. Sarukura, M. Hirano, *Appl. Phys. Lett.* **2001**, *78*, 2333.

32 K. Ueda, H. Hosono, *J. Appl. Phys.* **2002**, *91*, 4768; K. Ueda, K. Takafuji, H. Hiramatsu, H. Ohta, T. Kamiya, M. Hirano, H. Hosono, *Chem. Mater.* **2003**, *15*, 3692.

33 D. O. Charkin, A. V. Akopyan, V. A. Dolgikh, *Russ. J. Inorg. Chem.* **1999**, *44*, 833, and references therein.

34 H. Hiramatsu, K. Ueda, H. Ohta, M. Orita, M. Hirano, H. Hosono, *Appl. Phys. Lett.* **2002**, *81*, 598.

35 H. Hiramatsu, K. Ueda, K. Takafuji, H. Ohta, M. Hirano, T. Kamiya, H. Hosono, *J. Mater. Res.* **2004**, *19*, 2137.

36 H. Hiramatsu, H. Ohta, T. Suzuki, C. Honjo, Y. Ikuhara, K. Ueda, T. Kamiya, M. Hirano, H. Hosono, *Cryst. Growth Des.* **2004**, *4*, 301.

37 H. Hiramatsu, K. Ueda, H. Ohta, M. Hirano, T. Kamiya, H. Hosono, *Appl. Phys. Lett.* **2003**, *82*, 1048.

38 H. Hiramatsu, K. Ueda, K. Takafuji, H. Ohta, M. Hirano, T. Kamiya, H. Hosono, *J. Appl. Phys.* **2003**, *94*, 5805.

39 K. Ueda, H. Hiramatsu, H. Ohta, M. Hirano, T. Kamiya, H. Hosono, *Phys. Rev. B* **2004**, *69*, 155305.

40 H. Kamioka, H. Hiramatsu, H. Ohta, K. Ueda, M. Hirano, T. Kamiya, H. Hosono, *Appl. Phys. Lett.* **2004**, *84*, 879.

41 H. Kamioka, H. Hiramatsu, K. Ueda, M. Hirano, T. Kamiya, H. Hosono, *Opt. Lett.* **2004**, *29*, 1659.

42 H. Yanagi, T. Hase, S. Ibuki, K. Ueda, H. Hosono, *Appl. Phys. Lett.* **2001**, *78*, 1583.

43 K. Nomura, H. Ohta, K. Ueda, T. Kamiya, M. Hirano, H. Hosono, *Science* **2003**, *300*, 1269.

44 M. W. J. Prins, S. E. Zinnemers, J. F. M. Cillessen, J. B. Giesbers, *Appl. Phys. Lett.* **1997**, *70*, 458.

45 K. Nomura, H. Ohta, T. Suzuki, C. Honjo, K. Ueda, T. Kamiya, M. Orita, Y. Ikuhara, M. Hirano, H. Hosono, *J. Appl. Phys.* **2004**, *95*, 5532.

46 Y. Toda, S. Matsuishi, K. Hayashi, K. Ueda, T. Kamiya, M. Hirano, H. Hosono, *Adv. Mater.* **2004**, *16*, 685.

47 H. B. Bartl, T. Scheller, *Neues Jahrb. Mineral., Monatsh.* **1970**, *35*, 547.

48 R. W. Nurse, J. H. Welch, A. Majumdar, *Trans. Br. Ceram. Soc.* **1965**, *64*, 323.

49 H. Hosono, Y. Abe, *Inorg. Chem.* **1987**, *26*, 1192.

50 M. Lacerda, J. T. S. Irvine, F. P. Glasser, A. R. West,

Nature **1988**, *332*, 525.
51 H. Hosono, K. Yamazaki, Y. Abe, *J. Am. Ceram. Soc.* **1987**, *70*, 867.
52 H. Hosono, N. Asada, Y. Abe, *J. Appl. Phys.* **1990**, *67*, 2840.
53 H. Hosono, *Int. J. Appl. Ceram. Technol.* **2004**, *5*, 409.
54 K. Hayashi, M. Hirano, H. Hosono, *J. Mater. Res.* **2002**, *17*, 1244.
55 S. Watauchi, I. Tanaka, K. Hayashi, M. Hirano, H. Hosono, *J. Cryst. Growth* **2002**, *237*, 496.
56 Y. Toda, M. Miyakawa, K. Hayashi, T. Kamiya, M. Hirano, H. Hosono, *Thin Solid Films* **2003**, *445*, 309.
57 K. Hayashi, M. Hirano, S. Matsuishi, H. Hosono, *J. Am. Chem. Soc.* **2002**, *124*, 736.
58 K. Hayashi, S. Matsuishi, N. Ueda, M. Hirano, H. Hosono, *Chem. Mater.* **2003**, *15*, 1851.
59 S. Yang, J. N. Kondo, K. Hayashi, M. Hirano, K. Domen, H. Hosono, *Chem. Mater.* **2003**, *16*, 104.
60 K. Hayashi, S. Matsuishi, M. Hirano, H. Hosono, *J. Phys. Chem. B* **2004**, *108*, 8920.
61 K. Hayashi, N. Ueda, M. Hirano, H. Hosono, *Solid State Ionics* **2004**, *179*, 89.
62 S. Matsuishi, K. Hayashi, M. Hirano, I. Tanaka, H. Hosono, *J. Phys. Chem. B* **2004**, *108*, 8920.
63 S. Yang, J. N. Kondo, K. Hayashi, M. Hirano, K. Domen, H. Hosono, *Appl. Catal. A* **2004**, *277*, 234.
64 Q. Li, K. Hayashi, M. Nishioka, H. Kashiwagi, M. Hirano, Y. Torimoto, H. Hosono, M. Sadakata, *Appl. Phys. Lett.* **2002**, *80*, 4259.
65 K. Hayashi, M. Hirano, Q. Li, M. Nishioka, M. Sadakata, Y. Torimoto, S. Matsuishi, H. Hosono, *Electorochem. Solid-State Lett.* **2002**, *5*, J13.
66 Q. Li, K. Hayashi, M. Nishioka, H. Kashiwagi, M. Hirano, Y. Torimoto, H. Hosono, M. Sadakata, *Jpn. J. Appl. Phys.* **2002**, *41*, L530.
67 Q. Li, H. Hosono, M. Hirano, K. Hayashi, M. Nishioka, H. Kashiwagi, Y. Torimoto, M. Sadakata, *Surf. Sci.* **2003**, *527*, 100.
68 K. Hayashi, S. Matsuishi, T. Kamiya, M. Hirano, H. Hosono, *Nature* **2002**, *419*, 462.
69 K. Hayashi, Y. Toda, T. Kamiya, M. Hirano, I. Tanaka, T. Yamamoto, H. Hosono, *Appl. Phys. Lett.* **2005**, *86*, 22109.
70 P. V. Sushko, A. L. Shluger, K. Hayashi, M. Hirano, H. Hosono, *Phys. Rev. Lett.* **2003**, *91*, 126401.
71 P. V. Sushko, A. L. Shluger, K. Hayashi, M. Hirano, H. Hosono, *Thin Solid Films* **2003**, *445*, 161.
72 P. V. Sushko, A. L. Shluger, K. Hayashi, M. Hirano, H. Hosono, *Appl. Phys. Lett.* **2005**, *86*, 92101.
73 L. Dye, *Inorg. Chem.* **1997**, *36*, 3817.
74 S. Matsuishi, Y. Toda, M. Miyakawa, K. Hayashi, M. Hirano, I. Tanaka, H. Hosono, *Science* **2003**, *301*, 626.
75 Y. Toda, S. Matsuishi, K. Hayashi, K. Ueda, T. Kamiya, M. Hirano, H. Hosono, *Adv. Mater.* **2004**, *16*, 685.
76 M. Miyakawa, K. Hayashi, M. Hirano, Y. Toda, T. Kamiya, H. Hosono, *Adv. Mater.* **2003**, *15*, 1100.
77 M. Miyakawa, Y. Toda, K. Hayashi, T. Kamiya, M. Hirano, N. Matsunami, H. Hosono, *J. Appl. Phys.* **2005**, *97*, 23510.
78 S.-W. Kim, M. Miyakawa, K. Hayashi, M. Hirano, H. Hosono, *J. Am. Chem. Soc.* **2005**, *127*, 1370.
79 I. T. Godmanis, A. N. Trukhin, K. Hübner, *Phys. Status Solidi B* **1983**, *116*, 279.
80 D. L. Griscom, *J. Ceram. Soc. Jpn.* **1991**, *99*, 923.
81 K. Saito, A. J. Ikushima, *Phys. Rev. B* **2000**, *62*, 8584.
82 L. Skuja, H. Hosono, M. Hirano, K. Kajihara, *Proc. SPIE* **2003**, *5112*, 2.
83 *Defects in SiO_2 and Related Dielectrics: Science and Technology, NATO Science Series*, ed. by G. Pacchioni, L. Skuja, D. L. Griscom, Kluwer Academic Publishers, Dordrecht, Netherlands, **2000**.
84 L. Skuja, H. Hosono, M. Hirano, *Proc. SPIE* **2001**, *4347*, 155.
85 F. L. Galeener, *J. Non-Cryst. Solids* **1982**, *49*, 53.
86 R. A. B. Devine, R. Dupree, I. Farnan, J. J. Capponi, *Phys. Rev. B* **1987**, *35*, 2560.
87 N. Kitamura, K. Fukumi, K. Kadono, H. Yamashita, K. Suito, *Phys. Rev. B* **1994**, *50*, 132.
88 H. Hosono, Y. Ikuta, T. Kinoshita, K. Kajihara, M. Hirano, *Phys. Rev. Lett.* **2001**, *87*, 175501.
89 H. Hosono, Y. Ikuta, *Nucl. Instrum. Methods Phys. Res., Sect. B* **2000**, *166–167*, 691.
90 K. Kajihara, Y. Ikuta, M. Hirano, H. Hosono, *Appl. Phys. Lett.* **2002**, *81*, 3164.
91 K. Kajihara, Y. Ikuta, M. Hirano, H. Hosono, *J. Non-Cryst. Solids* **2003**, *322*, 73.
92 K. Kajihara, L. Skuja, M. Hirano, H. Hosono, *Appl. Phys. Lett.* **2001**, *79*, 1757.
93 Y. Morimoto, S. Nozawa, H. Hosono, *Phys. Rev. B* **1999**, *59*, 4066.
94 K. Kajihara, L. Skuja, M. Hirano, H. Hosono, *Phys. Rev. Lett.* **2002**, *89*, 135507.
95 Y. Ikuta, K. Kajihara, M. Hirano, S. Kikugawa, H. Hosono, *Appl. Phys. Lett.* **2002**, *80*, 3916.
96 Y. Ikuta, K. Kajihara, M. Hirano, H. Hosono, *Appl. Opt.* **2004**, *43*, 2332.
97 T. A. Michalske, S. W. Freiman, *J. Am. Ceram. Soc.* **1983**, *66*, 284.
98 T. E. Tsai, D. L. Griscom, *Phys. Rev. Lett.* **1991**, *67*, 2517.
99 L. Zhang, V. A. Mashkov, R. G. Leisure, *Phys. Rev. B* **1996**, *53*, 7182.
100 H. Hosono, H. Kawazoe, N. Matsunami, *Phys. Rev. Lett.* **1998**, *80*, 317.
101 K. Watanabe, *Adv. Geophys.* **1958**, *5*, 153.
102 L. Skuja, B. Güttler, *Phys. Rev. Lett.*, **1996**, *77*, 2093.
103 L. Skuja, M. Hirano, H. Hosono, *Phys. Rev. Lett.* **2000**, *84*, 302.
104 L. Skuja, K. Kajihara, T. Kinoshita, M. Hirano, H. Hosono, *Nucl. Instrum. Methods Phys. Res., Sect. B* **2002**, *191*, 127.
105 G. Pacchioni, G. Ieranó, *Phys. Rev. B* **1997**, *56*, 7304.
106 M. A. Szymanski, A. L. Shluger, A. M. Stoneham, *Phys. Rev. B* **2001**, *63*, 224207.
107 A. Bongiorno, A. Pasquarello, *Phys. Rev. Lett.* **2002**, *88*, 125901.
108 K. Kajihara, L. Skuja, M. Hirano, H. Hosono, *Phys. Rev. Lett.* **2004**, *92*, 015504.
109 L. Skuja, *J. Non-Cryst. Solids* **1994**, *179*, 51.
110 H. Hosono, K. Kajihara, T. Suzuki, Y. Ikuta, L. Skuja, M. Hirano, *Solid State Commun.* **2002**, *122*, 117.
111 T. Suzuki, L. Skuja, K. Kajihara, M. Hirano, T. Kamiya, H. Hosono, *Phys. Rev. Lett.* **2003**, *90*, 186404.
112 M. Cannas, F. M. Gelardi, *Phys. Rev. B* **2004**, *69*, 153201.
113 K. Kajihara, Y. Ikuta, M. Hirano, T. Ichimura, H. Hosono, *J. Chem. Phys.* **2001**, *115*, 9473.
114 K. Kajihara, Y. Ikuta, M. Hirano, H. Hosono, *Phys. Chem. Glasses C* **2002**, *43*, 137.

115 H. Hosono, M. Mizuguchi, H. Kawazoe, T. Ogawa, *Appl. Phys. Lett.* **1999**, *74*, 2755.
116 M. Mizuguchi, L. Skuja, H. Hosono, T. Ogawa, *J. Vac. Sci. Technol., B* **1999**, *17*, 3280.
117 Y. Hibino, H. Hanafusa, *J. Appl. Phys.* **1986**, *60*, 1797.
118 K. F. Klein, R. Arndt, G. Hillrichs, M. Ruetting, M. Veidemanis, R. Dreiskemper, J. Clarkin, G. Nelson, *Proc. SPIE* **2001**, *4253*, 42.
119 R. K. Brimacombe, R. S. Taylor, K. E. Leopold, *J. Appl. Phys.* **1989**, *66*, 4035.
120 M. Oto, S. Kikugawa, N. Sarukura, M. Hirano, H. Hosono, *IEEE Photon Technol. Lett.* **2001**, *13*, 978.
121 M. Oto, S. Kikugawa, T. Miura, M. Hosono, H. Hosono, *J. Non-Cryst. Solids* **2004**, *349*, 133.
122 G. Crowford, *Flexible Flat Panel Displays*, John Wiley & Sons, New York, **2005**.
123 K. Nomura, H. Ohta, A. Takagi, T. Kamiya, M. Hirano, H. Hosono, *Nature* **2004**, *432*, 488.
124 H. Hosono, M. Yasukawa, H. Kawazoe, *J. Non-Cryst. Solids* **1996**, *203*, 334.
125 H. Hosono, N. Kikuchi, N. Ueda, H. Kawazoe, *J. Non-Cryst. Solids* **1996**, *198–200*, 165.
126 S. Narushima, K. Ueda, H. Mizoguchi, H. Ohta, M. Hirano, K. Shimizu, T. Kamiya, H. Hosono, *Adv. Mater.* **2003**, *15*, 1409.
127 T. Kamiya, S. Narushima, H. Mizoguchi, K. Shimizu, K. Ueda, H. Ohta, M. Hirano, H. Hosono, *Adv. Funct. Mater.* **2005**, *15*, 968.
128 S. Narushima, M. Hiroki, K. Ueda, K. Shimizu, T. Kamiya, M. Hirano, H. Hosono, *Philos. Mag. Lett.* **2004**, *84*, 665.
129 A. Takagi, K. Nomura, H. Ohta, H. Yanagi, T. Kamiya, M. Hirano, H. Hosono, *Thin Solid Films* **2005**, *486*, 38.

Award recipient

Hideo Hosono was born in Kawagoe, Saitama prefecture in 1953. He received B.E. in 1977 and Ph.D. in 1982 both from Tokyo Metropolitan University. He was appointed as a research associate at Nagoya Institute of Technology in 1982 and was promoted to an associate professor at department of inorganic materials, NIT. During 1989–90, he studied ion-implantation into amorphous SiO_2 with Prof. Robert A. Weeks at Vanderbilt University, TN, U. S. A. In 1993, he moved to Tokyo Institute of Technology and was promoted to a professor at Materials and Structures Laboratory, Tokyo Tech in 1999 via an associate professorship at the Institute of Molecular Science at Okazaki. He was appointed the current position on October 1, 2004. He has served the leader of *Hosono Transparent Electro-Active Materials Project* (1999–2004), ERATO, Japan Science and Technology Agency (JST) and is leading the MEXT 21st Century COE program "*Nanomaterials Cultivation for Industrial Collaboration*" (2002–2007) and JST ERATO-SORST project "*Function Cultivation of Transparent Oxides Utilizing Nano-Structure and Their Application*" (2004–2009). His current research focus is novel function exploration in wide-gap crystalline and amorphous oxides utilizing built-in nanostructure and defect manipulation.

Dr. Toshio Kamiya received B.S. degree in 1990 and Dr. degree in 1996 from Tokyo Institute of Technology. He joined Department of Inorganic Materials of Tokyo Institute of Technology in 1991 as a research associate. He worked on ferroelectric ceramics and computer simulation of oxide crystals till 1996 and received the Dr.(Eng.) degree. From 1996 to 2002, he studied growth and device applications of silicon thin films. He joined Microelectronics Research Centre, Cavendish Laboratory of University of Cambridge from 2000 to 2002 and worked on single-electronics. In 2002, he joined Materials and Structures Laboratory of Tokyo Institute of Technology as an assistant professor and is serving as an associate professor since 2003. He was with the ERATO *Hosono Transparent Electro-Active Materials (TEAM) Project* by Japan Science and Technology Agency and is also serving a group leader in the ERATO-SORST TEAM project.

Dr. Masahiro Hirano received B.S. degree in 1966, M.S. degree in 1968 and Dr. degree in 1971 from Tokyo University. He joined Electrotechnical Laboratory of MITI in 1971. He was with Optoelectronic Industry and Technology Association from 1981 to 1984 and Optoelectronic Joint Research Laboratory from 1984 to 1987. He worked for Asahi Glass Company from 1988 to 1999. He jointed ERATO *Hosono Transparent Electro-Active Materials (TEAM) Project* by Japan Science and Technology Agency in 1999. He is now with ERATO-SORST TEAM project. He is also Professor of 21st Century COE project of Tokyo Institute of Technology.